Small Molecules as Amyloid Inhibitors: Molecular Dynamic Simulations with Human Islet Amyloid Polypeptide (IAPP)

Kelsie King

Thesis submitted to the faculty of the Virginia Polytechnic Institute and State University in partial fulfillment of the requirements for the degree of

Master of Science in Life Science
In
Biochemistry

Thesis Committee
Anne M. Brown, Chair
Justin A. Lemkul
Richard F. Helm

April 13, 2021
Blacksburg, VA

Keywords: amyloids, islet amyloid polypeptide, flavonoids, molecular dynamics simulations, drug discovery

Small Molecules as Amyloid Inhibitors: Molecular Dynamic Simulations with Human Islet Amyloid Polypeptide (IAPP)

Kelsie King

ACEDEMIC ABSTRACT

Islet amyloid polypeptide (IAPP) is a 37-residue amyloidogenic hormone implicated in the progression of Type II Diabetes (T2D). T2D affects an estimated 422 million people yearly and is a co-morbidity with numerous diseases. IAPP forms toxic oligomers and amyloid fibrils that reduce pancreatic β-cell mass and exacerbate the T2D disease state. Toxic oligomer formation is attributed, in part, to the formation of inter-peptide β-strands comprised of residues 23-27 (FGAIL). Flavonoids, a class of polyphenolic natural products, have been found experimentally to inhibit IAPP aggregate formation. Many of these known IAPP aggregation attenuating small flavonoids differ structurally only slightly; the influence of functional group placement on inhibiting the aggregation of the $IAPP_{(20-29)}$ has yet to be explored. To probe the role of small-molecule structural features that impede IAPP aggregation, molecular dynamics (MD) simulations were performed on a model fragment of $IAPP_{(20-29)}$ in the presence of morin, quercetin, dihydroquercetin, epicatechin, and myricetin. Contacts between Phe23 residues are critical to oligomer formation, and small-molecule contacts with Phe23 are a key predictor of β-strand reduction. Structural properties influencing the ability of compounds to disrupt Phe23-Phe23 contacts include carbonyl and hydroxyl group placement. These structural features influence aromaticity and hydrophobicity, principally affecting ability to disrupt $IAPP_{(20-29)}$ oligomer formation. This work provides key information on design considerations for T2D therapeutics.

Small Molecules as Amyloid Inhibitors: Molecular Dynamic Simulations with Human Islet Amyloid Polypeptide (IAPP)

Kelsie King

GENERAL AUDIENCE ABSTRACT

Type II Diabetes (T2D) affects an estimated 422 million people worldwide, with the World Health Organization (WHO) reporting that approximately 1.5 million deaths were directly caused by T2D in 2019. The progression of T2D has been attributed to a protein, called islet amyloid polypeptide (IAPP, or amylin) that is co-secreted with insulin after individuals eat or consumes calories. IAPP has been discovered to form toxic aggregates or clumps of protein material that worsen the disease state and cause a loss of mass of pancreatic cells. There is a large market for therapeutics of T2D and more small molecule drugs are needed to slow progression and severity of T2D. Flavonoids, a class of natural molecules, have been found to inhibit the processes by which IAPP promotes T2D disease progression by stopping the aggregation of IAPP. The structures of these flavonoid compounds differ slightly but show difference in ability to slow IAPP aggregation. By understanding how those differences confer more or less protection against T2D and inhibit IAPP aggregation, we can design more potent and specific drugs to target IAPP. To probe the role of molecular structure in preventing IAPP aggregation, molecular dynamics (MD) simulations — a powerful computational technique — were performed on a model fragment of IAPP in the presence of molecules morin, quercetin, dihydroquercetin, epicatechin, and myricetin. MD simulations provide extremely detailed information about potential drug interactions with a given target, serving as an important tool in the development of new drugs. This work has identified key features and predictors of effective IAPP drugs, providing a framework for the further development of therapeutics against T2D and similar diseases.

Acknowledgements

First and foremost, I would like to thank my advisor, Dr. Anne Brown, for the constant support and direction she has provided me. I would also like to thank my committee members, Dr. Justin Lemkul and Dr. Richard Helm, for providing critical feedback throughout my research. I would like to thank the entirety of the Bevan & Brown Lab - in particular, I would like to thank my fellow graduate students Amanda Sharp and Erin Collins, for their support throughout this process, as well as Dan Chen, Carter Gottschalk and R. Jason Moiser for their assistance in statistics and visualization. I acknowledge and thank Advanced Research Computing at Virginia Tech for providing access to the supercomputing resources provided by Cascades and New River computing clusters. I thank my parents, Diane Toney and James King. Lastly, I would like to thank Danny Zawatsky and Patrick Torchia.

Table of Contents

‘

Attributions
All chapters in this thesis were written by Kelsie M. King. Edits and guidance was provided by Dr. Anne M. Brown. Attributions are detailed below.

Authors for this document are as follows:
Kelsie M. King (KMK)
Dr. David R. Bevan (DRB)
Dr. Anne M. Brown (AMB)

Chapter 1
Attribution: KMK organized and wrote this section with input on edits and corrections from AMB.

Chapter 2
Attribution: AMB and KMK designed experimental protocol and built MD systems, KMK performed the MD simulations, analysis, visualization, and statistical analysis with input from AMB. KMK wrote the chapter with edits and direction from AMB, and suggestions from DRB.

Chapter 3
Attribution: KMK wrote the chapter with edits and direction from AMB.

Chapter 1 Introduction

1.1 Amyloid Diseases

Amyloid proteins are characterized by the formation of elongated, β-sheet rich aggregates[1]. These proteins have normal physiological functions, but often are prone to misfolding, either by way of incorrect cleavage or high concentration[1]. These misfolded proteins have been implicated in several diseases, including Alzheimer's disease, Parkinson's disease, and Type II Diabetes (T2D) **(Table 1.1).** Amyloid fibrils generally share a common structure, exhibiting a cross-β-spine rich in β-sheets running parallel to the fibril axis[2]. These insoluble fibers are stable are not believed to induce toxicity; rather, soluble oligomers formed on-pathway to aggregation[3]. Thus, it is of interest to find ways to disrupt the process of aggregation to innovate in the drug design space. This work focuses on inhibition of islet amyloid polypeptide (IAPP) — considered to be the most amyloidogenic protein[4, 5] — to develop design considerations for new therapeutics for T2D.

Table 1.1 List of common amyloid diseases and their associated amyloidogenic protein.

Disease	Protein
Alzheimer's Disease	Amyloid-β peptide (Aβ)
Huntington's disease	Huntingtin
Parkinson's disease	α-synuclein
Rheumatoid arthritis	Serum amyloid A
Type II Diabetes	Islet amyloid polypeptide (IAPP)

1.2 Islet amyloid polypeptide (IAPP) in Type II Diabetes (T2D)

Islet amyloid polypeptide (IAPP), or amylin, is a 37-residue hormone secreted with insulin by islet pancreatic β-cells. IAPP is involved primarily in metabolic regulation; some physiological roles include signaling post-meal satiation[6], controlling gastric emptying[7], and control of glucagon release[8]. The 37-residue peptide formed from three sequential cleavages: 1) from an 89-residue preproprotein to the 67-residue proislet amyloid polypeptide (proIAPP) in the endoplasmic reticulum[9], 2) two cleavages at the N- and C-termini in the secretory granules[9]. The C-terminus of IAPP is amidated, and a disulfide bond between residues Cys2 and Cys7 result in the biologically active IAPP[10, 11].

IAPP in its monomeric state is a soluble, intrinsically disordered protein[12]. When secreted in high concentrations, as in T2D, this protein is highly amyloidogenic, and forms β-sheet, fibrillar aggregates deposited on pancreatic β-cells[13]. Increased concentration of IAPP has been linked to reduced pancreatic β-cell mass[14]. Interestingly, fully formed amyloid fibrils are not the primary toxic species; rather, low-molecular weight oligomers are thought to exert their cytotoxic effects[3, 15]. The exact mechanism by which these prefibrillar species induce cytotoxicity is not well understood; however, a growing body of evidence suggests that oligomers form ion-permeable pores capable of disrupting membranes[16, 17]. It has been suggested that interactions with ER membranes can lead to calcium ion leakage, inducing apoptosis[3, 18]. Thus, it is of interest to understand the process of oligomerization so that compounds can be developed to stabilize or prevent their formation.

1.3 The Influence of Residues 20-29 ($IAPP_{(20-29)}$) in Oligomerization and Fibril Formation

Most amyloid proteins are comprised of a hydrophobic core that drives fibril formation[19]. These regions across amyloidogenic proteins differ in their primary sequence but share common structural features. For instance, 1-2 aromatic residues are commonly found in the hydrophobic core of several amyloidogenic proteins[20], suggesting that π-π interactions are critical in fibril formation **(Table 1.2)**. In the case of IAPP, aggregation is driven by residues 20-29 (SNNFGAILSS)[21]. A study by Zanni *et. al.* utilizing 2D IR spectroscopy revealed that IAPP oligomerization was primarily driven by the formation of transient, parallel β-sheets comprising residues 23-27[21]. Ultimately, these β-sheets are thermodynamically unfavorable; β-strand structure in residues 23-27 collapse into disordered loop regions connecting β-strands formed by flanking polar residues. These oligomeric intermediates then nucleate then nucleate the formation of amyloid fibrils[22].

Table 1.2 The hydrophobic core regions of several amyloidogenic proteins. Aromatic residues are underlined. Sequences from Azriel *et. al.* and Rodriguez *et. al.*

Disease	Protein	Amyloidogenic Sequence
Alzheimer's disease	Amyloid-β peptide (Aβ)	KLV<u>FF</u>AE
Creutzfeldt-Jakob disease	PrP	PHGGG<u>W</u>GQ
Rheumatoid arthritis	Serum amyloid A	S<u>FF</u>S<u>F</u>LGEA<u>F</u>D
Type II Diabetes	Islet amyloid polypeptide (IAPP)	SNN<u>F</u>GAILSS

The importance of IAPP residues 20-29 is highlighted when examining differences in aggregation propensity across IAPP orthologues. For instance, rat IAPP (rIAPP) is classified as non-amyloidogenic[23]. rIAPP and human IAPP differ in six residue positions, with 5 of those differences occurring in the 20-29 region **(Figure 1.1)**. In rIAPP, substitutions for proline occur at residues 25, 28, and 29[23]. Proline generally disrupts the formation of β-sheets and α-helices, suggesting the formation of β-sheets in the 20-29 region is critical for IAPP oligomerization.

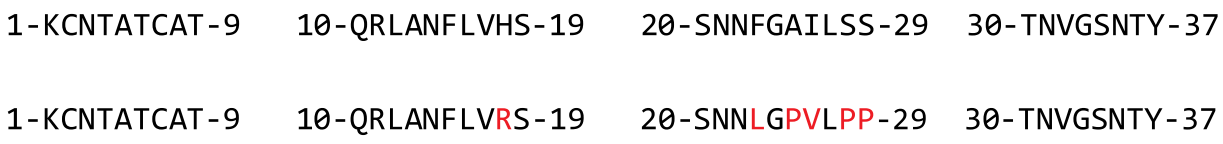

Figure 1.1 Sequences of (top) human IAPP and (bottom) rat IAPP. Residues differing from human IAPP are colored in red.

1.4 Flavonoids as Amyloid Inhibitors

Flavonoids are a class of secondary plant metabolites that are commonly found in diets that exhibit a host of beneficial attributes, such as antioxidant[24], anti-inflammatory[25], and anti-carcinogenic properties[26]. Epidemiological studies have identified diets high in polyphenols to confer protection against T2D[27, 28]. Thus, these compounds became of interest in the search for inhibitors against IAPP and other amyloidogenic diseases. As such, these compounds have been found to inhibit IAPP and other amyloidogenic proteins through ThT fluorescence assays and transmission electron microscopy (TEM)[29-32]. These polyphenolic compounds have several properties that give rise to their inhibitory properties; namely, the presence of catechol groups, which are important for hydrogen bonding and covalent mechanisms[32], and their ability to π-stack with key aromatic residues[33].

1.5 Mechanisms of Flavonoid Inhibition of IAPP Aggregation

The mechanism by which flavonoids modify IAPP aggregates varies by molecule. For example, morin hydrate was reported to prevent fibril formation fibril formation[34], resveratrol destabilizes helical intermediates[35], and epigallocatechin gallate (EGCG) redirects oligomers to off-pathway structures[36]. However, there are commonalities in regard to their interactions with the peptide.

1.5.1 Covalent Mechanisms

Covalent mechanisms of inhibition have been observed for flavonoids found to disrupt IAPP aggregation. Catechol groups have been specifically identified as the features of compounds that are more likely and more effectively able to form covalent adducts with amine-containing side chains when compared with other molecules[32]. Catechol groups can readily undergo oxidation to form o-quinone intermediates in this mechanism, which could explain their higher efficacy compared to other compounds[32]. Dihydroquercetin (taxifolin)[37] and baicalein[38] are two compounds proposed to inhibit Aβ and IAPP, respectively, via covalent adduct formation.

1.5.2 Non-Covalent Mechanisms

Noncovalent inhibition mechanisms have been attributed to hydrophobic interactions[39, 40], with an emphasis on π-stacking interactions between flavonoids and aromatic residues[41, 42]. The aromatic features may exert their inhibitory effects by disrupting inter-peptide interactions between aromatic residues, which are thought to be important for fibril formation[43, 44]. In addition to hydrophobic interactions, backbone hydrogen bonding may play a role in the disruption of aggregate formation[45]. This is notable, as backbone hydrogen bonding may play a key role in stability of fibrils[46, 47].

Chapter 2 Molecular Dynamics Simulations Indicate Aromaticity as a Key Factor in $IAPP_{(20-29)}$ Inhibition

Kelsie King[1], David R. Bevan[1,3], and Anne M. Brown[1,2,3].

Department of Biochemistry,[1] University Libraries,[2] and Virginia Tech Center for Drug Discovery[3] Virginia Tech, Blacksburg, VA 24061

2.1 Abstract

Islet amyloid polypeptide (IAPP) is a 37-residue amyloidogenic hormone implicated in the progression of Type II Diabetes (T2D), affecting an estimated 422 million people. IAPP forms toxic oligomers and amyloid fibrils that reduce pancreatic β-cell mass and exacerbate the T2D disease state. IAPP oligomerization is believed to be driven by the formation of inter-peptide β-strands comprised of residues 23-27 (FGAIL). Flavonoids, a class of polyphenolic natural products, have been found experimentally to inhibit aggregate formation. Many of these small molecules differ in structure only slightly; the influence of functional group placement on inhibiting the aggregation of the $IAPP_{(20-29)}$ has yet to be explored. To probe the role of small-molecule structural features in amyloid inhibition, molecular dynamics (MD) simulations were performed on a model fragment of $IAPP_{(20-29)}$ in the presence of morin, quercetin, dihydroquercetin, epicatechin, and myricetin. Contacts between Phe23 residues are critical to oligomer formation, and small-molecule contacts with Phe23 are a key predictor of β-strand reduction. Chemical properties influencing the ability of compounds to disrupt Phe23-Phe23 contacts include carbonyl and hydroxyl group placement. These structural features influence aromaticity and hydrophobicity, principally affecting a compounds ability to disrupt $IAPP_{(20-29)}$ oligomer formation. This work provides key information on design considerations for T2D therapeutics.

2.2 Introduction

Type 2 diabetes (T2D), classified as noninsulin-dependent diabetes, is a complex metabolic disorder affecting over 400 million people worldwide[48], with an estimated direct patient cost of $827 billion[49]. T2D is typically characterized by insulin resistance and and impaired pancreatic β-cell function[50]. As T2D progresses, a transition from a compensated phase of insulin resistance to a decompensated phase that consists of hyperinsulinemia and hyperglycemia occurs[51]. Islet amyloid polypeptide (IAPP), or amylin, is a 37-residue hormone co-secreted with insulin by pancreatic β-cells[52, 53] and is implicated in the decompensated phase of T2D[54]. Specifically, in T2D, excess IAPP is found in amyloid-like aggregate deposits in and around pancreatic β-cells. IAPP aggregates — particularly oligomers[3] — are known to contribute to the loss of properly functioning β-cells, causing deteriorated glycemic control[55], higher rates of monotherapy failure[51, 56], and ultimately exacerbating T2D pathogenesis. Oligomers have been proposed to induce their cytotoxic effects via various mechanisms, including β-cell membrane perturbation[57] and ion channel formation[51, 56], and ultimately exacerbating T2D pathogenesis. Oligomers have been proposed to induce their cytotoxic effects via various mechanisms, including β-cell membrane perturbation[57] and ion channel formation[17]. Consequently, it is critical to study the oligomerization process such that therapeutics for T2D can be developed that specifically attenuate the aggregation and fibrilization of IAPP.

IAPP fibrilization is driven by residues 20-29 (SNNFGAILSS), a region often referred to as the “hydrophobic core”[21]. This residue region initiates the IAPP aggregation process by forming oligomers comprised of transient, parallel β-sheets comprised of

residues 23-27 (FGAIL)[21]. This structural intermediate is thermodynamically unfavorable; ultimately, β-strand structure in residues 23-27 collapse into disordered loop regions connecting β-strands formed by flanking polar residues[21]. These oligomeric intermediates then nucleate into amyloid fibrils[22]. Given the importance of residues 20-29 in oligomer formation of full-length IAPP, and their apparent cytoxoticity[3], it is of interest to develop a model system of $IAPP_{(20-29)}$ to characterize the formation of β-sheets in this region. Characterization of $IAPP_{(20-29)}$ aggregation can give insight into key interactions between potential inhibitors and the peptide, informing the design of therapeutics for T2D.

Flavonoids are a class of secondary plant metabolites that are commonly found in diets that exhibit a host of beneficial attributes, such as antioxidant[24], anti-inflammatory[25], and anti-carcinogenic properties[26]. These polyphenolic compounds are of interest in drug discovery pipelines and have been found to inhibit IAPP aggregation *in vitro*[29-32]. Flavonoids share a common structural backbone, consisting of two phenyl rings (A and B) and a heterocyclic C ring **(Figure 2.1)**. Curiously, flavonoids such as morin, quercetin, and myricetin, share this backbone, but have shown differences in their ability to inhibit IAPP via thioflavin-T (ThT) fluorescence assays and transmission electron microscopy (TEM)[32, 34]. Herein, determining the chemical features that most influence the ability to inhibit IAPP is necessary for the development of better therapeutics against T2D. To probe the influence of a flavonoid molecular structure on its ability inhibit IAPP aggregation, atomistic-resolution data is necessary. In this regard, molecular dynamics (MD) provide information that can be difficult to obtain experimentally, serving as an important tool in the development of potential new inhibitors[58].

Here, we utilize MD simulations to create a model system of $IAPP_{(20-29)}$ to probe the aggregation process and formation of a trimer. Additionally, to probe the influence of small molecules on attenuating the aggregation process, we have deigned an experiment series (Figure 2.1) that characterizes key inter-peptide interactions that must be disrupted for IAPP aggregate formation and provide a deeper understanding of the structural and chemical properties required for effective IAPP aggregate inhibition. Simulations were performed with three $IAPP_{(20-29)}$ fragments, representing the amyloidogenic core of the protein, with five small molecules rich in the phenolic groups deemed important for amyloid inhibition: morin (MOR), quercetin (QUR), dihydroquercetin (DHQ), myricetin (MYR), and epicatechin (EPI) **(Figure 2.1)**. Utilization of the $IAPP_{(20-29)}$ fragment can serve as a computationally inexpensive model system to study key inter-peptide contacts in this region that can be extrapolated to the full-length peptide. The simulated compounds share a 15-member carbon scaffold, differing in positions of hydroxyl groups, carbonyl oxygen and aromaticity **(Figure 2.1)**. This work describes aggregation of a trimer of $IAPP_{(20-29)}$ and the impact of small molecule structural features on the resulting $IAPP_{(20-29)}$ structural morphologies, giving new insights into the structural and chemical properties necessary for effective IAPP inhibition.

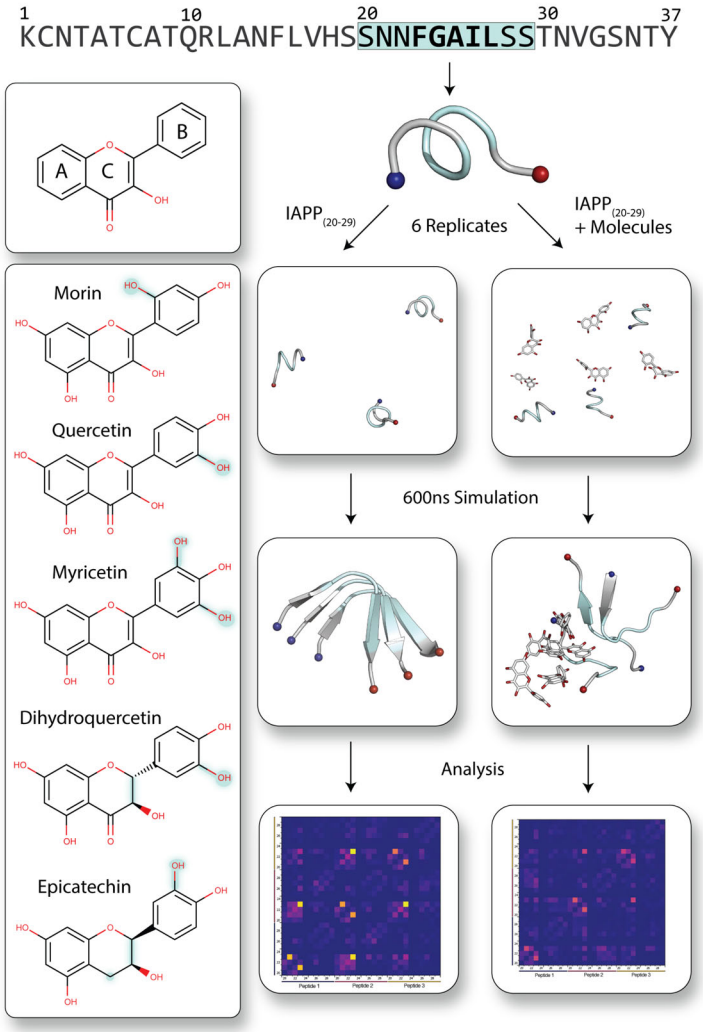

Figure 2.1 Schematic overview of simulation construction and design. Islet amyloid polypeptide (IAPP) residues 20-29 were isolated from PDB ID: 2I86[15] and simulated for 600 ns in the presence of five small molecules (left). Hydroxyl groups and changes in ring C distinguishing each molecule are highlighted in light teal. $IAPP_{(20-29)}$ is depicted as cartoon. The N- and C-termini of $IAPP_{(20-29)}$ are shown as spheres and colored blue and red, respectively. Residues 23-29 (FGAIL) are highlighted in blue. Small molecule (morin for this example) is shown as sticks.

2.3 Methods

2.3.1 $IAPP_{(20-29)}$ Peptide Generation and Small Molecule Parameterization

The full length IAPP system was constructed using GROMACS version 4.6.5[59] with the GROMOS96 53A6 forcefield[60]. PDB ID: 2l86 was utilized as the IAPP starting structure[61]. The $IAPP_{(20-29)}$ fragment was obtained as described by Ling *et al.* to obtain a structure representative of IAPP an aqueous solution[62]. Briefly, full-length IAPP from PDB ID: 2L86[61] was simulated for 600 ns and residues 20-29 were extracted from a dominant morphology after cluster analysis. Fragment N- and C-termini were acetylated and amidated, respectively. Small molecule topologies were generated using the PRODRG[63] server and refined as described by Lemkul *et. al*[64] with morin as a source molecule. Quercetin, myricetin, dihydroquercetin, and epicatechin were parameterized by analogy. Briefly, charges and charged groups were assigned based on functional groups available in the GROMOS96 53a6 parameter set[60]. Ether and ketone groups are not available in this set; charges for these functional groups were utilized as described by Stubbs *et. al.*[65], and van der Waals parameters were assigned from GROMOS96 atom types. For simulations of mutant $IAPP_{(20-29)}$ (F23L), the 20-29 fragment was isolated directly from PDB ID: 2L68 and Phe23 was replaced with leucine using PyMOL[66] before system construction.

2.3.2 System Construction and MD Simulations

Three $IAPP_{(20-29)}$ identical fragments were placed in an 11 x 11 x 11 nm cubic box, with a minimum solute-box distance of 1.0 nm, and solvated with SPC water[67]. Seven systems were constructed. One control simulation was constructed containing only three peptides, while simulations with flavonoids were constructed with a 5:3 flavonoid:peptide

ratio. Simulations with F23L similarly contained three peptides. Peptides and flavonoids were placed at least 2+ nm apart from the closest interacting atoms to reduce potential for interaction biases. To give a net-neutral system and to mimic physiological conditions, the trimer was simulated with 150 mM NaCl with additional counterions. Energy minimization was performed using the steepest descent method, where heavy atoms were restrained. Energy minimization was followed by equilibration, using NVT and NPT ensembles. Six replicates were generated in NVT, each with random starting velocities for each system. Velocities were assigned from the Maxwell distribution. NVT was applied to the systems for 100 ps with the Berensden weak coupling method[68], with the temperature held constant at 310 K. Following NVT, NPT was applied to the systems for 100 ps with the Nosé-Hoover thermostat[69, 70] and Parrinello-Rahman barostat[71, 72], held at a constant pressure of 1 bar, and with a reference temperature of 310 K. For NPT, new velocities were not assigned and were continued from NVT application. All bonds were constrained with the Linear Constraint Solver (LINCS)[73] with an integration step of 2 fs. Following equilibration, MD simulations were performed with released heavy-atom restraints. The short-range electrostatic interaction cutoff was 0.9 nm, and the short-range van der Waals cutoff was 1.4 nm. The Particle Mesh Ewald (PME)[74, 75] method was used to compute long-range electrostatic interactions, using cubic interpolation and a Fourier grid space[74] of 0.16 nm. Three-dimensional periodic boundary conditions (PBC) were applied. Simulations were performed for 600 ns for each replicate per system, for a total simulation time of 25.2 μs. Simulation input files and parameters are available on the Bevan & Brown Lab OSF page (https://osf.io/82n73/)[76].

2.3.3 Analysis

Simulations were performed over 600 ns and replicates displayed convergence based on backbone root-mean-square deviation (RMSD) over the last 200 ns of simulation time **(Figures S1-S7).** Thus, all system averages presented in this work are taken over the last 200 ns of simulation for a total sample time of 8.4 μs. All data generation and analysis was carried out using GROMACS version 2018.1[77] functions and in-house Python 3.7 programs. RMSD clustering was performed using the Gromos[78] method, with an RMSD cut-off of 0.2 nm. Surface mapping and property prediction was performed using Schrodinger Maestro[79]. Molecular visualization was performed using PyMOL[66].

2.3.4 Statistical Testing

All statistical testing was performed with R. Most datasets generated were found to violate assumptions of equal variance and normally distributed residuals necessary for parametric statistical tests. Thus, statistical significance tests were performed using the non-parametric methods. For multi-level datasets (>2), Kruskal-Wallis (KW) tests were used in conjunction with Dunn's KW Multiple Comparisons test for post-hoc pairwise difference testing. Statistical tests between two groups were performed using the Mann-Whitney test. Statistical difference was defined as $P < 0.05$.

2.4 Results and Discussion

Simulations were performed with three $IAPP_{(20\text{-}29)}$ fragments in the presence of small molecules (morin, quercetin, myricetin, dihydroquercetin, and epicatechin) to observe inhibition of oligomer formation. Given that secondary structure changes in the 20-29 region drive cytotoxic oligomer formation[21], disruptions in this region can be extrapolated to the full-length peptide. Thus, the 20-29 model allows us to study the

efficacy of flavonoids against full-length IAPP using a more computationally inexpensive system. Through observing oligomer formation, we sought to 1) identify key inter-peptide contacts driving $IAPP_{(20-29)}$ trimerization, and 2) identify structural features of flavonoids that may give rise to more effective inhibition of $IAPP_{(20-29)}$ oligomerization.

2.4.1 Disruption of inter-peptide Phe23 contacts are critical in inhibiting $IAPP_{(20-29)}$ trimerization

Secondary structure is an important metric in assessing both ability of the $IAPP_{(20-29)}$ model to adapt structural morphologies determined experimentally and probe the efficacy of compounds to disrupt on-pathway aggregation. As such, careful consideration was made in selecting a force field to model $IAPP_{(20-29)}$ trimer formation. The GROMOS96 53a6 forcefield has been shown to model β-strand formation of the amyloidogenic amyloid-β (Aβ) peptide in agreement with experimental data, with other force fields tending to over-stabilize α-helices[80]. Fibrilization of Aβ and IAPP both follow the sigmoidal kinetics of amyloid formation[81], and have been reported to cross-aggregate via amyloidogenic cores[82, 83, 80]. Thus, by analogy, this force field and experimental design is suitable to model the amyloidogenic $IAPP_{(20-29)}$ fragment and probe the ability of this fragment to form inter-peptide β-strand structure that can be compared to full-length IAPP aggregates. To assess the secondary structure of $IAPP_{(20-29)}$ trimers, RMSD clustering was performed to visualize representative structures over the last 200 ns of simulation. $IAPP_{(20-29)}$ trimers tended to adopt two distinct morphologies: 1) in-register, parallel β-sheets, and 2) disordered trimers exhibiting both β-sheet and random coil structure **(Figure 2.2, Figure S8)**. Residues 23-27 in full length IAPP have been shown through 2D IR spectroscopy experiments to form parallel, in-register β-sheets that transition to

disordered loops[21]. The $IAPP_{(20-29)}$ trimers are observed to sample both conformations, supporting the use of an $IAPP_{(20-29)}$ fragment model in simulations.

Experimental studies utilizing circular dichroism (CD) spectroscopy describe a reduction in β-strand content for IAPP and similar amyloids, such as Aβ and α-synuclein, in the presence of effective inhibitors, resulting in nontoxic, off-pathway oligomers[36, 84]. Thus, β-strand structure reduction can be used as a metric for assessing inhibition efficacy. Dominant morphologies from clustering show $IAPP_{(20-29)}$ to be more disordered in the presence of the compounds simulated **(Figure 2.2, Figures S9-S14)**. To quantify this observation, secondary structure was calculated using the DSSP algorithm[85] (Table 1). The β-strand content of $IAPP_{(20-29)}$ was significantly lower ($P < 0.05$ for all replicates) in the presence of each compound, adopting primarily random coil structure **(Table 2.1, Figure S15)**. Furthermore, statistical differences in β-strand structure were observed depending on the molecule present, ranking as follows: Quercetin (19 ± 5) = Myricetin (18 ± 5) < Morin (28 ± 5) < Dihydroquercetin (31 ± 9) < Epicatechin (40 ± 6). β-strand content in the presence of morin or quercetin was not statistically different ($p = 0.07$). The variation of β-strand structure of $IAPP_{(20-29)}$ in the presence of different small molecules highlights the ability to discern atomistic level interactions and changes due to the small molecule present. Inasmuch, we can hypothesize about the chemical properties that would offer more effective amyloid aggregate inhibition.

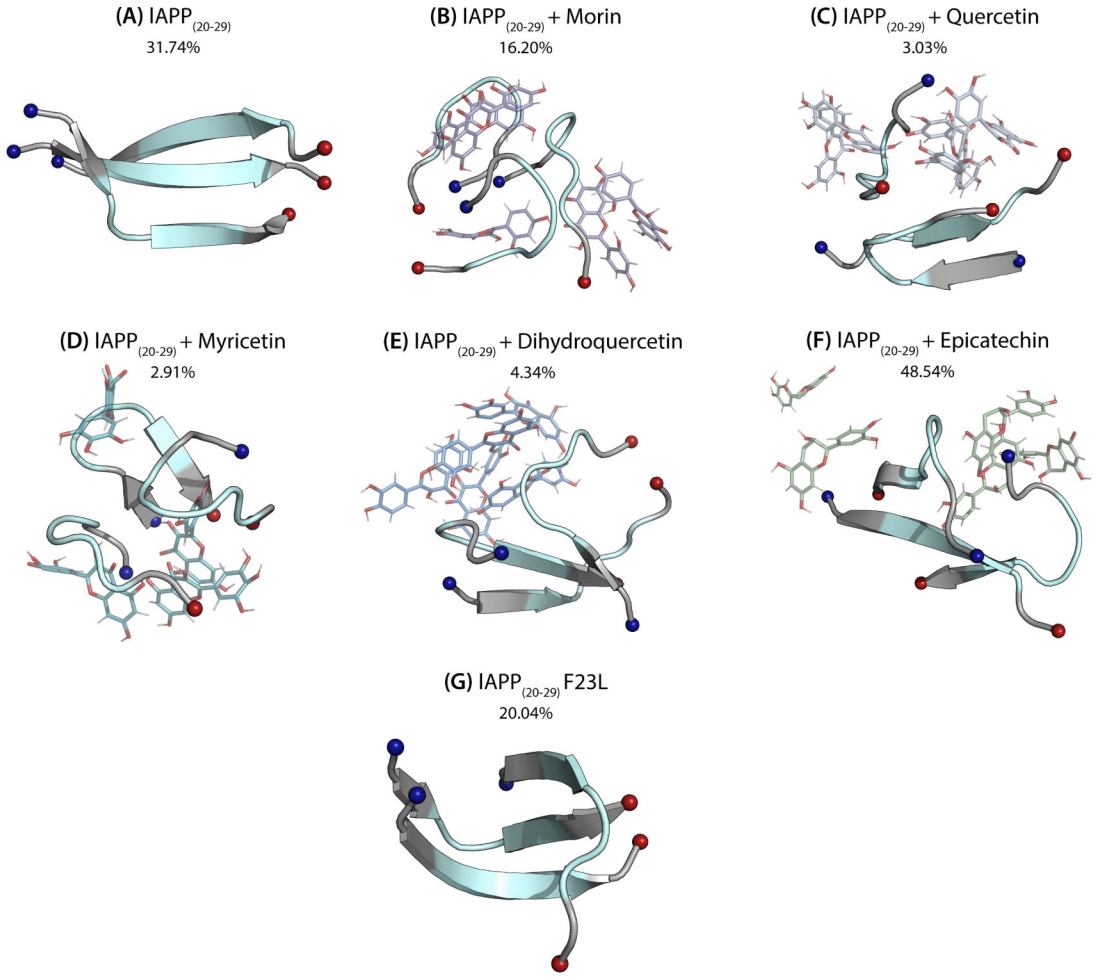

Figure 2.2 Representative structures from RMSD clustering of (A) $IAPP_{(20-29)}$, and $IAPP_{(20-29)}$ in the presence of (B) morin, (C) quercetin, (D) myricetin, (E) dihydroquercetin, (F) epicatechin, and (G) $IAPP_{(20-29)}$ Phe23LEU mutant (F23L). Dominant morphologies of $IAPP_{(20-29)}$ in the presence of small molecules tend more disordered, adopting larger percentages of random coil structure. Structures were obtained from backbone RMSD clustering over the last 200 ns of simulation. The structures shown are from replicates with the lowest root-mean-square deviation (RMSD) with respect to all other replicates. Peptides are shown as cartoon, with residues 23-27 (FGAIL) colored as teal. N- and C-termini are shown as spheres and colored as blue and red, respectively. Small molecules are shown as sticks, with oxygens colored red. Percentages indicate the2 percentage of frames the structure represents over the last 200 ns of simulation time.

Table 2.1 Average secondary structure and standard deviation across all replicates for $IAPP_{(20-29)}$ and $IAPP_{(20-29)}$ + small molecule systems. Averages taken over the last 200 ns of simulation and represent averages across all peptides and all replicates.

System	Coil (%)	β-Strand (%)	Helix (%)
$IAPP_{(20-29)}$	43 ± 5	57 ± 5	0 ± 0
$IAPP_{(20-29)}$ + Morin	72 ± 5	28 ± 5	0 ± 0
$IAPP_{(20-29)}$ + Quercetin	81 ± 5	19 ± 5	0 ± 0
$IAPP_{(20-29)}$ + Myricetin	82 ± 5	18 ± 5	0 ± 0
$IAPP_{(20-29)}$ + Dihydroquercetin	69 ± 9	31 ± 9	0 ± 0
$IAPP_{(20-29)}$ + Epicatechin	60 ± 6	40 ± 6	0 ± 0
$IAPP_{(20-29)}$ F23L	50 ± 5	50 ± 5	0 ± 0

To probe the influence of compounds on β-strand structure reduction, residue-residue interaction frequency maps were created to determine which inter-peptide interactions were maintained or lost in the presence of a given molecule **(Figures S15-S20)**. $IAPP_{(20-29)}$ exhibited the highest frequency of interaction between Phe23 residues. This inter-peptide contact was significantly reduced in the presence of each compound **(Table 2.2)**. Interestingly, Phe23 contact frequency is well correlated with β-strand structure content (R^2 = 0.91). We then questioned how strongly β-strand formation could be correlated with a given residue-residue interaction. Contacts between Phe23 residues can be more closely associated with $IAPP_{(20-29)}$ β-strand structure than other residue-residue contact **(Table S1)**. This suggests that disrupting interactions between Phe23 residues is critical in inhibiting the 20-29 fragment trimer formation, with experimental fragments[86] and full-length IAPP[84] studies in agreement with the potential role of Phe23 on aggregation ability.

Studies with full-length IAPP also suggest this may be a key residue target for small molecules; Tang *et. al.* demonstrated the ability of the cardiovascular disease drug cloridarol to inhibit IAPP β-strand structure and cytotoxicity *in vitro*[84]. MD simulations of cloridarol with full-length IAPP suggested that interactions with Phe23, as well as Leu27 and Asn31 were of high probability.

Table 2.2 Average number of Phe23-Phe23 contacts for $IAPP_{(20-29)}$ and $IAPP_{(20-29)}$ + small molecule systems. P-values indicate statistical difference from $IAPP_{(20-29)}$ trimer with no small molecules present. Averages were taken over the last 200 ns of simulation and represent averages across all peptides and all replicates.

System	Average Number of Phe23-Phe23 Contacts	P-Value
$IAPP_{(20-29)}$	25 ± 11	--
$IAPP_{(20-29)}$ + Morin	8 ± 5	0.009
$IAPP_{(20-29)}$ + Quercetin	4 ± 2	0.002
$IAPP_{(20-29)}$ + Myricetin	5 ± 3	0.003
$IAPP_{(20-29)}$ + Dihydroquercetin	9 ± 5	0.01
$IAPP_{(20-29)}$ + Epicatechin	10 ± 3	0.01

Mutation of aromatic IAPP residues in both fragment[87] and full-length[88, 89] studies slows fibrilization kinetics, but does not prevent amyloid formation. To further probe the role of Phe23 in $IAPP_{(20-29)}$ trimerization, simulations were performed with mutant Phe23Leu fragments (referred to as F23L). β-strand structure was reduced between $IAPP_{(20-29)}$ (57 ± 5) and $IAPP_{(20-29)}$ F23L (50 ± 5) **(Table 2.1)**. Representative structures

from RMSD clustering indicate that F23L tends to form anti-parallel β-sheets, implying that Phe23 plays a role in fibril directionality **(Figure S21)**[42]. Furthermore, F23L exhibited fewer intramolecular interactions, as shown by radius of gyration and contact frequency calculations. The average radius of gyration for F23L peptides (1.8 ± 0.7) was greater than $IAPP_{(20-29)}$ (1.4 nm ± 0.4), suggesting the mutation results in reduced peptide packing. Furthermore, residue-residue contact frequency maps indicate F23L peptides have lower interaction affinities, displaying no clear preference for a particular residue-residue contact **(Figure S21)**. These data support the conclusion that Phe23 plays a critical role in the formation of $IAPP_{(20-29)}$ trimers with characteristics of on-pathway aggregates. The study of F23L aggregation in the presence of small molecules is warranted to further probe the role of Phe23 contact disruption in $IAPP_{(20-29)}$ inhibition. Simulations are currently underway with F23L in the presence of quercetin.

The molecules studied here are polyphenolic, containing 2-3 aromatic ring systems capable of interacting with Phe23 through π-π stacking. Dominant morphologies show that the aromatic rings of each small molecule interact with Phe23 in various π-stacking configurations **(Figure S22)**. Considering that β-strand structure is highly correlated with inter-peptide Phe23 interactions, we hypothesized that contact frequency between an inhibitor and Phe23 is predictor for $IAPP_{(20-29)}$ oligomerization. Contact frequencies between $IAPP_{(20-29)}$ sidechains and each compound were calculated to examine affinities for particular residues **(Figure 2.3)**. Each small molecule exhibits a preference for interactions with Phe23 over other residues; however, probability of Phe23 interaction varied by system. Ranking for compound-Phe23 interaction probabilities are as follows: Quercetin (0.92) > Dihydroquercetin (0.78) > Myricetin (0.62) > Morin (0.57) > Epicatechin

(0.39). Linear regression to correlate small molecule Phe23 interaction probability with β-strand structure reduction was performed (R^2 = 0.79), however, this is not in complete agreement with disruption of inter-peptide Phe23 interactions (R^2 = 0.91). However, quercetin displays the highest frequency of interaction with Phe23 and induces the largest β-strand structure reduction with respect to the $IAPP_{(20-29)}$ trimer (-38%). Conversely, epicatechin induces the smallest β-strand reduction with respect to $IAPP_{(20-29)}$ (-17%), while exhibiting the smallest Phe23 affinity by a significant margin. This suggests that direct interaction with Phe23 is a factor in β-strand reduction, but not as important as simple disruption of the inter-peptide contact.

Differences in β-strand structure, inter-peptide Phe23-Phe23 contacts, and compound-Phe23 interactions have been identified as metrics for assessing the efficacy of each simulated compound. Using these metrics, we propose a ranking among the inhibitors: 1) quercetin, 2) myricetin, 3) morin, 4) dihydroquercetin, and 5) epicatechin **(Table 2.3)**. Having constructed a relative ranking system, comparisons between compounds can be made to identify structural features that give rise to more effective inhibitory properties.

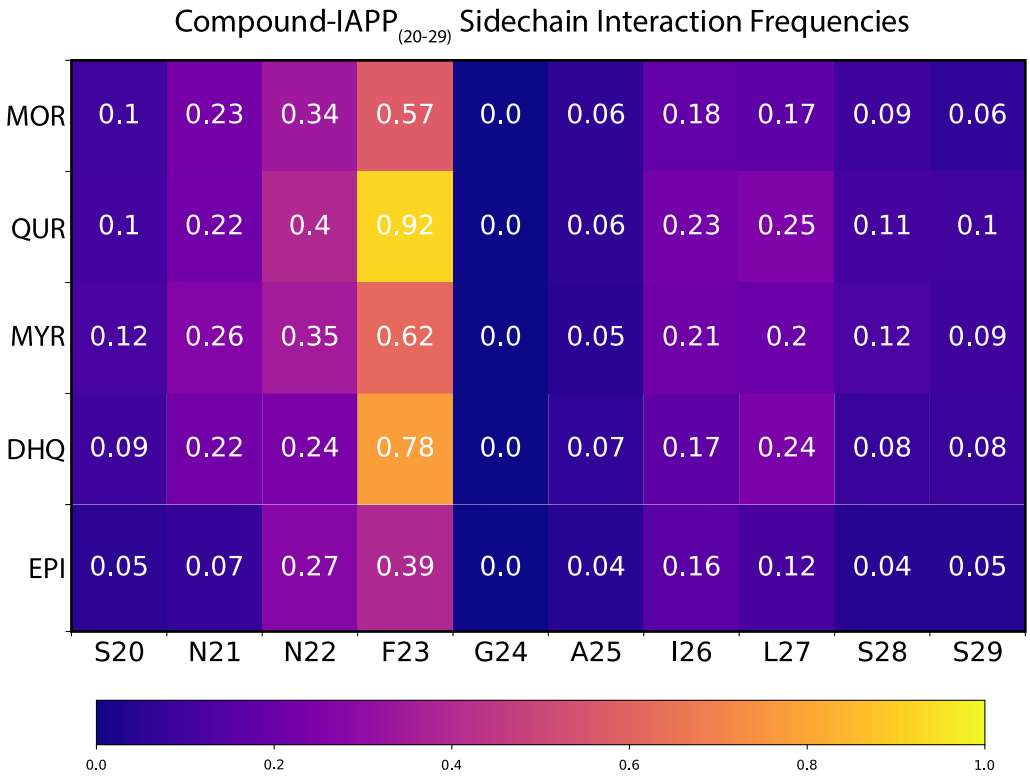

Figure 2.3 Interaction frequency (probability) maps between IAPP$_{(20-29)}$ sidechains and small molecules morin (MOR), quercetin (QUR), myricetin (MYR), dihydroquercetin (DHQ), and epicatechin (EPI). Frequencies represent the average across all peptides and all replicates. Frequency was calculated by taking the average number of sidechain-sidechain contacts within 0.6 nm over the last 200 ns of simulation divided by the number of interactors (sum of atoms between both residue sidechains).

Table 2.3 Ranking system for efficacy of simulated small molecules in inhibiting IAPP(20-29) trimerization. Ranking metrics based on β-strand percentage, inter-peptide Phe23 interaction frequency, and frequency of interaction between Phe23 and compound. Ranked from 1 (most effective) to 5 (least effective).

Ranking	System	β-strand %	PHE23-PHE23 Interaction Frequency	Compound-PHE23 Interaction Frequency
1	$IAPP_{(20-29)}$ + QUR	19 ± 5	0.12	0.92
2	$IAPP_{(20-29)}$ + MYR	18 ± 5	0.15	0.62
3	$IAPP_{(20-29)}$ + MOR	28 ± 5	0.23	0.57
4	$IAPP_{(20-29)}$ + DHQ	31 ± 9	0.25	0.78
5	$IAPP_{(20-29)}$ + EPI	40 ± 6	0.29	0.39

2.4.2 Carbonyl oxygen and vicinal hydroxyls are key features for attenuating $IAPP_{(20-29)}$ oligomer formation

The compounds studied here have been found experimentally to inhibit amyloid fibril formation[32, 37, 90]. Sharing a common 15-carbon backbone, these aromatic compounds structurally differ with respect to placement of hydroxyl groups and carbonyl oxygens, as well as in their aromaticity **(Figure 2.1)**. Differences in $IAPP_{(20-29)}$ β-strand content depending on the compound present were observed and is discussed above. As such, it is of interest to understand the influence of these structural features on $IAPP_{(20-29)}$ inhibition efficacy.

Several studies have attributed inhibitory activity against IAPP fibrilization to aromatic interactions[84, 91, 92]. Given that inter-peptide Phe23 contact disruption can be associated with β-strand reduction, it is likely that compound aromaticity is an important factor for $IAPP_{(20-29)}$ inhibition. Interaction frequencies between $IAPP_{(20-29)}$ sidechains and small molecule functional groups ring were calculated, highlighting interesting differences in Phe23 affinities **(Figures S23-S27)**. Epicatechin — whose β-strand structure reduction

was the smallest compared to control $IAPP_{(20-29)}$ among the simulated compounds — exhibits a reduced probability of interacting with Phe23 via its C-ring compared to other molecules **(Figure 2.4A)**. The epicatechin C-ring is the least aromatic of the compounds simulated, lacking both a double bond and a carbonyl substituent in the heterocyclic C-ring **(Figure 2.1)**, and is thus unlikely to participate in π-interactions via this ring. Considering epicatechin exhibited the smallest β-strand structure compared to other molecules, this suggests that C-ring aromaticity may influence inhibition efficacy.

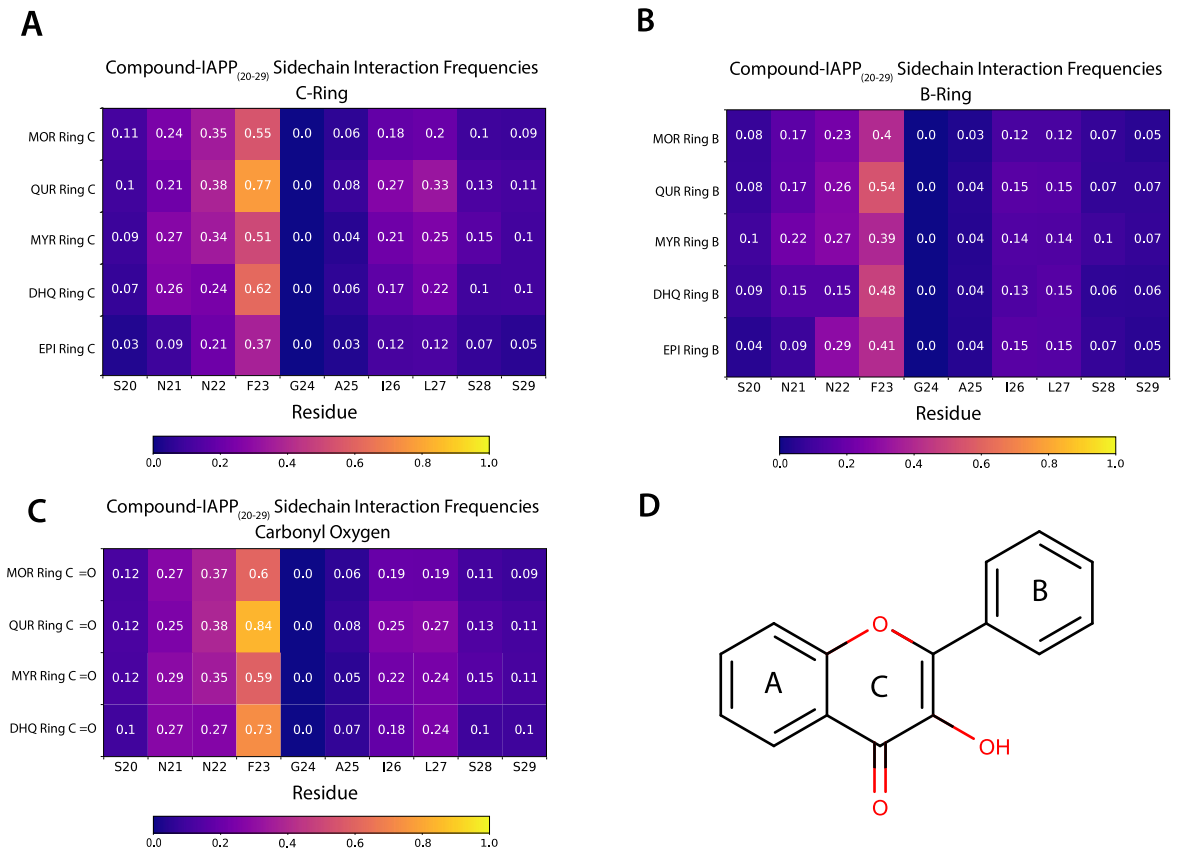

Figure 2.4 Interaction frequency (probability) maps between $IAPP_{(20-29)}$ sidechains and **(A)** heterocyclic C-rings, **(B)** B-rings, and **(C)** C-ring carbonyl oxygens for morin (MOR), quercetin (QUR), myricetin (MYR), dihydroquercetin (DHQ), and epicatechin (EPI) (no carbonyl oxygen for EPI). **(D)** General flavonoid scaffold, with A, B, and C rings labelled.

Dihydroquercetin, like epicatechin, lacks a C-ring double bond **(Figure 2.1)**. However, this compound exhibited an increased probability of interacting with Phe23 via the C-ring, and a larger β-strand structure reduction (-26%) compared to epicatechin (-17%) **(Figure 2.4A).** Interaction frequency maps show dihydroquercetin has a higher probability of interacting with Phe23 via this carbonyl oxygen compared to morin and myricetin (0.73, 0.60, and 0.59, respectively). Furthermore, the dihydroquercetin C-ring has a higher probability of interaction with Phe23 than that of epicatechin **(Figure 2.4C and 2.4D)**. This suggests that the carbonyl oxygen plays a role in aromaticity, and thus facilitates interactions with Phe23. The lack of aromaticity in the epicatechin C-ring is reflected in its flexibility compared to the other compounds; C-ring carbons appear to be puckering out-of-plane more so than other compounds **(Figure S29)**. While electronic effects are not accounted for in an additive force field such as GROMOS 53a6, we hypothesize that this structural feature bolsters π-electron density in the C-ring, resulting in a more planar structure. This is supported by chemical shift anisotropy estimations performed with Jaguar from Schrödinger Maestro[93]. Anisotropy was used in this context to estimate the π-electron density at a given atom. Morin, quercetin, dihydroquercetin, and myricetin had similar anisotropies at the 4-carbon position (1.47-1.89), while epicatechin was estimated to be much lower (0.25) **(Figure S29)**. While these estimations may explain a phenomenon observed in our simulations, it must be noted that further investigation using a polarizable or quantum mechanical force field would be necessary to confirm the role of π-electron density in compound-Phe23 interaction. An alternative explanation could be that the carbonyl oxygen engages in π-interactions with Phe23. Carbonyl-π interactions

have been identified across several crystal structures and may be important for stabilizing secondary structures[94].

It has been experimentally determined that self-aggregate forming small molecules are effective amyloid inhibitors[95, 96]. Praveen *et al.* determined that the polyphenolic compound resveratrol stabilized off-pathway IAPP oligomers via aromatic residue interactions, self-associating through hydrogen bonds and π-π interactions[96]. Structures from RMSD clustering of $IAPP_{(20-29)}$ in the presence of epicatechin often showed the compound spread across the simulation box, a phenomenon not seen in the other systems **(Figure S30).** Given that epicatechin reduced β-strand structure the least of all compounds simulated, we hypothesized that molecule self-association may be an important factor in $IAPP_{(20-29)}$ inhibition. The average radius of gyration (R_g), a measure of compactness, was calculated for small molecules over the last 200 ns of simulation **(Table 2.4)**. Epicatechin packed less tightly with itself than any small molecule (3.1 ± 0.5 nm), suggesting that self-association is important for effective inhibition.

Conversely, morin was found to be the most compact compound on average (1.9 ± 0.7 nm). Interestingly, morin displayed the second lowest probability of interacting with Phe23 (0.57) **(Figure 2.3)**. This suggests that while compound self-association is important, there is an ideal range of self-association that optimizes interactions between small molecules and with the peptide for more effective inhibition. Morin is the only simulated compound containing *meta*-oriented B-ring hydroxyls, which may influence aromaticity and hydrophobicity of the compound. To probe this, QikProp from Schrödinger Maestro[79] was used to estimate the π-carbon solvent accessible surface area (SASA) and logP of each compound **(Table 2.4)**. Interestingly, morin has the highest π-carbon

SASA of the compounds (239 $Å^2$) and has the highest logP (1.54). This increased aromaticity and hydrophobicity may facilitate stronger inter-molecular interactions at the expense of interactions with the peptide. For example, extensive B-ring stacking was seen in structures from RMSD clustering **(Figure S30)**; additionally, this compound displayed a diminished probability of interacting with Phe23 via the B-ring **(Figure 2.4)**. Interestingly, the strongest self-aggregator was morin, who tends to engage in intra-molecular stacking via the B-ring **(Figure S30).** Given that morin differs from quercetin, the top ranked compound, only in B-ring hydroxylation (*meta*- and *ortho*- configurations, respectively), this suggests that vicinal hydroxyls are an ideal feature for effective inhibitors of $IAPP_{(20-29)}$ oligomerization.

Table 2.4 Average radius of gyration, average intra-molecular hydrogen bonds between small molecules (SM), and π-carbon solvent-accessible surface area (SASA) for small molecules. Averages represent that for all molecules, across all replicates.

Small Molecule (SM)	Average Radius of Gyration (nm)	π-Carbon SASA ($Å^2$)	logP
Morin	1.9 ± 0.7	239	1.54
Quercetin	2.2 ± 0.7	227	1.48
Myricetin	2.1 ± 0.8	196	1.42
Dihydroquercetin	2.3 ± 0.7	221	0.95
Epicatechin	3.1 ± 0.5	210	1.02

In addition to influencing aromaticity and hydrophobicity, B-ring hydroxylation influence hydrogen bonding with the peptide. Backbone hydrogen bonds are critical in

fibril formation, linking β-strand segments perpendicular to the fibril axis[81, 97]. Thus, disrupting hydrogen bonds between peptides may slow or prevent oligomer and later fibril formation. To probe the hydrogen bonding ability of each small molecule, the average number of hydrogen bonds between compounds and $IAPP_{(20-29)}$ were calculated over the last 200 ns of simulation **(Table 2.5)**. Hydrogen bonding capacity may explain the increased efficacy of myricetin in reducing β-strand structure compared to other compounds, despite displaying a lower probability of interaction with Phe23 (0.62) **(Figure 2.3)**. Myricetin contains an additional B-ring hydroxyl, and consequently engages in more hydrogen bonding with $IAPP_{(20-29)}$.

Table 2.5 Average hydrogen bonds between compounds and $IAPP_{(20-29)}$ over the last 200 ns of simulation.

Compound	Total Hydrogen Bonds	Backbone Hydrogen Bonds	Sidechain Hydrogen Bonds
Morin	8 ± 1	5 ± 1	3 ± 1
Quercetin	9 ± 1	6 ± 1	3 ± 1
Myricetin	10 ± 1	6 ± 1	4 ± 1
Dihydroquercetin	7 ± 1	5 ± 1	3 ± 1
Epicatechin	5 ± 1	2 ± 1	2 ± 1

2.4.3 Electron affinity and π-carbon SASA are predictors of IAPP inhibition

There is a large body of literature dedicated to the study of natural products as amyloid inhibitors[29, 33, 98]. Xu *et. al.* utilized high-throughput ThT fluorescence assays and transmission electron microscopy (TEM) to assess the efficacy of 28 natural products in inhibiting IAPP amyloid formation[32]. Efficacies of the compounds in reducing ThT fluorescence compared to the control varied greatly; thus, this data can be leveraged to

assess the validity of the features hypothesized to be important in this work (aromaticity, hydrophobicity). Property prediction using QikProp from Schrödinger Maestro was performed on 21 compounds utilized in this study. To identify structural and chemical differences between more and less effective compounds, molecules were grouped based on their ability to inhibit ThT fluorescence compared to the IAPP control (compounds displaying < 50% of control ThT fluorescence, and compounds displaying > 70% of control ThT fluorescence). Significant differences between groups were observed for π carbon solvent-accessible surface area (SASA) and hydrophobic SASA ($p = 0.01$ and $p=0.001$, respectively) **(Table 2.6)**. The differences in π-carbon SASA can be attributed to the difference in hydrophobic SASA, as no differences were observed for other SASA metrics. This supports the conclusion that there may be an ideal π-carbon SASA range and can be used as a key metric in the development of IAPP inhibitors.

Table 2.6 Values for SASA and electron affinity as predicted by Schrodinger QikProp. Compounds were separated into two groups: compounds exhibiting less than 50% of ThT fluorescence compared to IAPP control, and compounds exhibiting greater than 70% of compounds compared to IAPP control. Data for compounds performance compared to IAPP control was taken from Xu. *et. al.*

Property	**ThT Fluorescence < 50% Control**		**ThT Fluorescence > 70% Control**		***P-Value***
	Average	**Range**	**Average**	**Range**	
Total SASA (Å^2)	551 ± 153	(391, 953)	609 ± 192	(345, 902)	0.4
Hydrophobic SASA (Å^2)	26 ± 35	(0, 99)	233 ± 185	(64, 576)	0.001
Hydrophilic SASA (Å^2)	253 ± 116	(148, 536)	201 ± 108	(87, 395)	0.3
π-Carbon SASA (Å^2)	271 ± 56	(147, 347)	175 ± 95	(19, 312)	0.01
Electron Affinity (eV)	0.7 ± 0.3	(-0.1, 1.1)	0.08 ± 0.6	(-1.0, 0.9)	0.005

Another significant difference between groups was observed for estimated electron affinity ($p = 0.005$). Electron affinity is defined as the change in energy of a gaseous molecule when an electron is added. On average, the higher efficacy group exhibited higher electron affinity (0.7 ± 0.3 eV) than the lower efficacy group (0.08 ± 0.6 eV) **(Table 2.6)**. It should be noted that the accuracy of QikProp in calculating electron affinity has been questioned due to inconsistencies in experimental determination of this value[99]. However, the large difference and the trend may warrant the use of this metric in IAPP inhibitor development.

To further characterize the flavonoids probed in this work, property prediction was performed for each compound and compared to the averages from the higher-efficacy group. Regarding π-carbon SASA and electron affinity, both predicted values for quercetin and dihydroquercetin were within the range comparable to the more-effective inhibitor group **(Table 2.7)**. Quercetin exhibited the most interactions with Phe23, and largest average β-strand reduction of the compounds studied in this work. Thus, it is likely that these metrics have predictive power in assessing IAPP inhibition efficacy. Furthermore, this supports that $IAPP_{(20\text{-}29)}$ model is useful in predicting ability to inhibit full-length IAPP amyloid formation.

Table 2.7 Values for SASA and electron affinity as predicted by Schrodinger QikProp. Ideal range was calculated as one standard deviation from the average for the ThT Fluorescence < 50% control group (see table 2.6).

Compound	π-Carbon SASA (Å^2)	Hydrophobic SASA (Å^2)	Electron Affinity (eV)
Morin	239	0	1.3*
Quercetin	227	0	1.0
Myricetin	196*	0	0.9
Dihydroquercetin	221	0	0.9
Epicatechin	210*	60	0.3*
Ideal Range	(215, 327)	(0, 61)	(0.4, 1)

2.5 Conclusions

This work utilized MD simulations to probe the ability of five small molecules to inhibit the aggregation an $IAPP_{(20-29)}$ trimer. Inter-peptide Phe23 interactions are critical for β-strand formation characteristic of on-pathway aggregates. The compounds in this work inhibited inter-peptide Phe23 interactions principally through π interactions; as such, aromaticity is a key factor in assessing inhibition efficacy. Aromaticity, self-association, and π-carbonyl interactions increase Phe23 affinity. These metrics can be used to benchmark the efficacy of compounds when developing new IAPP inhibitors.

Chapter 3 Conclusions

To the best of our knowledge, at the time of submission, this is the first computational work observing oligomer formation in the presence of small molecules. Studies with small molecules have been performed utilizing the preformed fibril[100, 101], however, this does not give information about the effects of these compound on oligomer

formation. By simulating oligomer formation, we gain insights into the contacts involved in their formation, thereby informing important peptide-molecule contacts to disrupt oligomerization. Utilizing the 20-29 model, we have identified inter-peptide interactions between Phe23 to be critical for both oligomer formation and oligomer disruption. As such, we have identified aromaticity as a key factor in the efficacy of inhibition, proposing ideal ranges for properties such as π-carbon SASA to quantify this observation. Furthermore, this work has put forth a computationally efficient 20-29 fragment model in the study of small-molecule inhibition. With GPU acceleration, we have seen simulation speeds approaching 80 ns/day for currently running systems of comparable size. A potential application of this model could involve a high-throughput MD protocol simulating several more compounds with the fragment to put forth a truly systematic study on the influence of functional groups in inhibiting oligomerization.

Insights into the mechanisms of inhibition are difficult to achieve in traditional experiments. Amyloid proteins aggregate quickly, and often necessitate organic solvents to slow this process. Furthermore, experimental methods fail to resolve this information at resolutions of that found in MD simulation data. However, MD and computational techniques are not without their own limitations; force field selection is critical to properly model a given system, and classical MD fails to model covalent mechanisms. Here we have demonstrated that MD can reproduce observations made in experimental literature, and can be used as a tool to further the drug discovery space in regard to developing amyloid inhibitors.

4 Supplemental Information

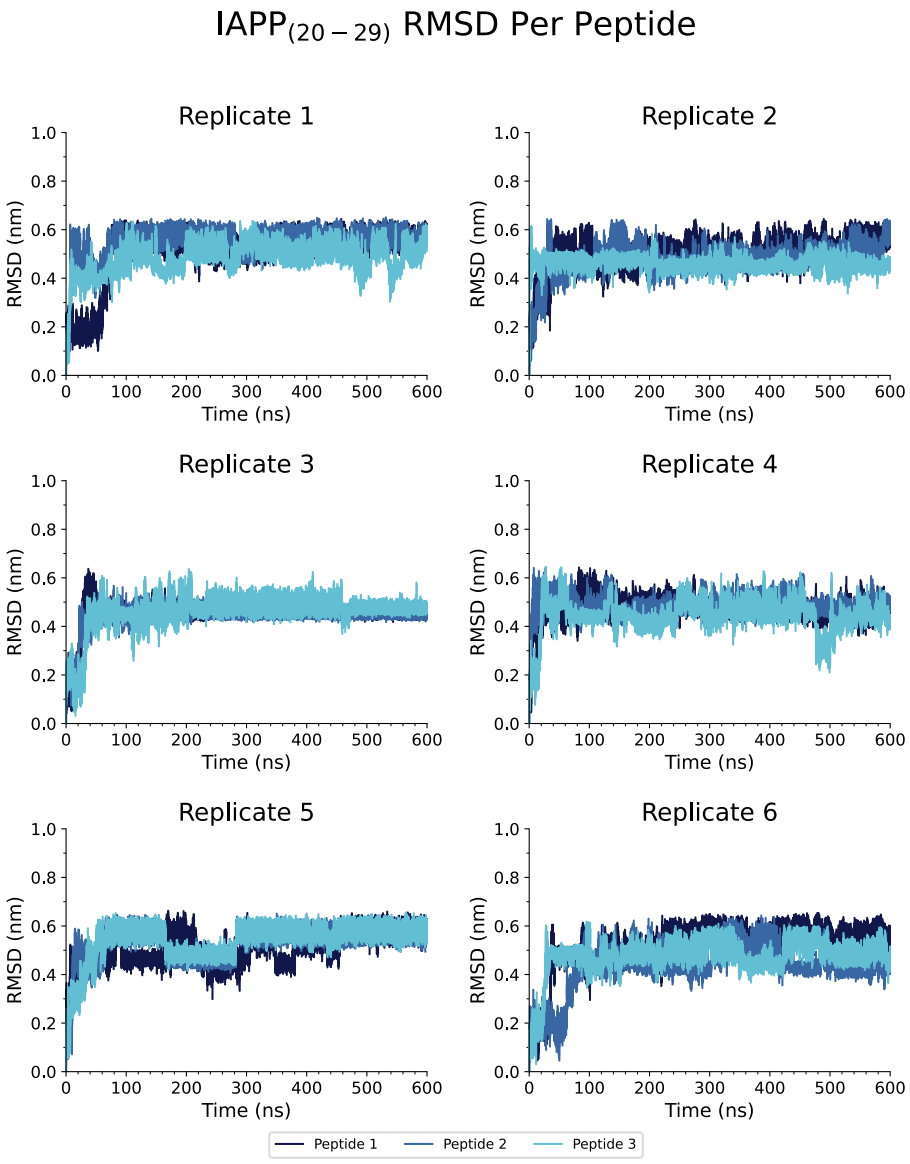

Figure S*1*: Root-mean-square deviation (RMSD) of $IAPP_{(20\text{-}29)}$ backbone atoms per peptide. RMSD of the trimer is calculated per peptide over time with starting positions as reference. Calculations performed for individual peptides, with peptide 1 shown as dark blue, peptide 2 shown as medium blue, and peptide 3 shown as light blue.

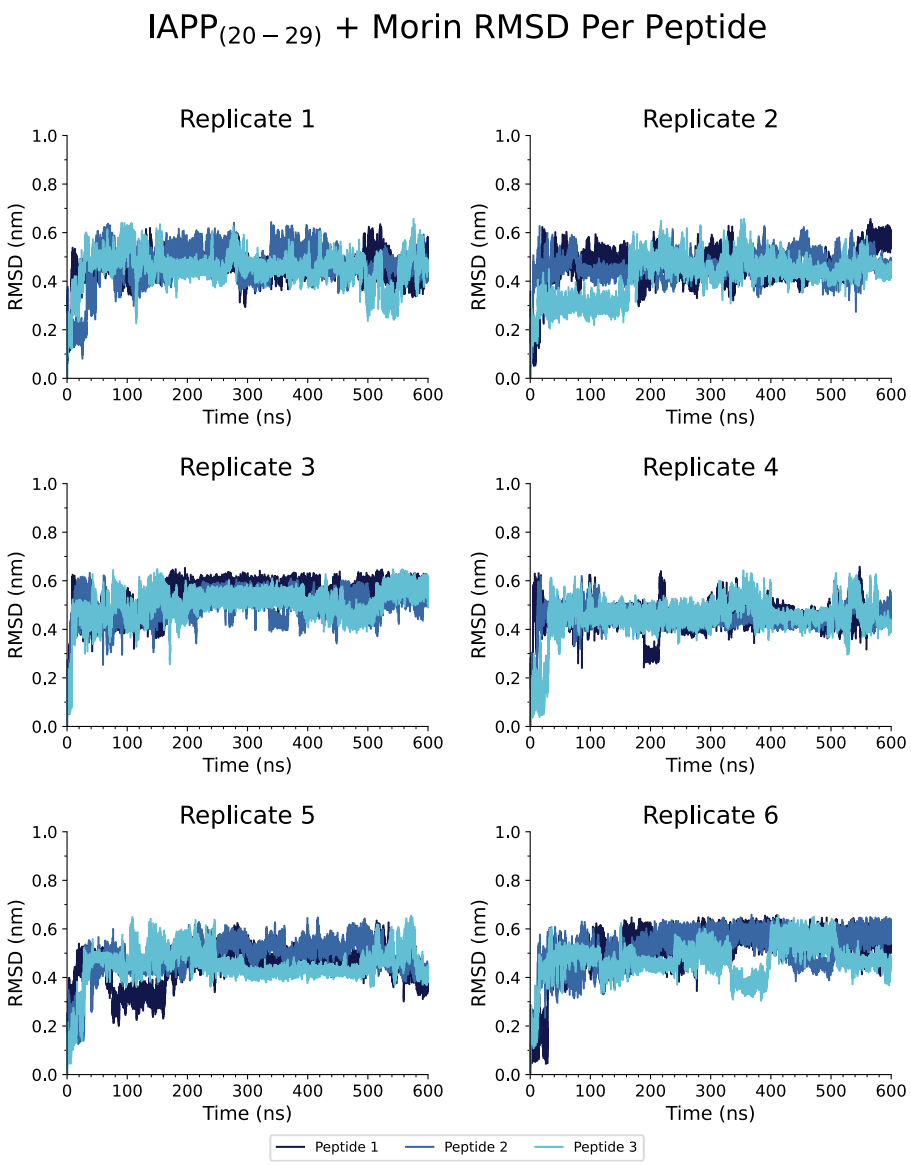

Figure S2: Root-mean-square deviation (RMSD) of $IAPP_{(20-29)}$ backbone atoms per peptide in the presence of morin. RMSD of the trimer is calculated per peptide over time with starting positions as reference. Calculations performed for individual peptides, with peptide 1 shown as dark blue, peptide 2 shown as medium blue, and peptide 3 shown as light blue.

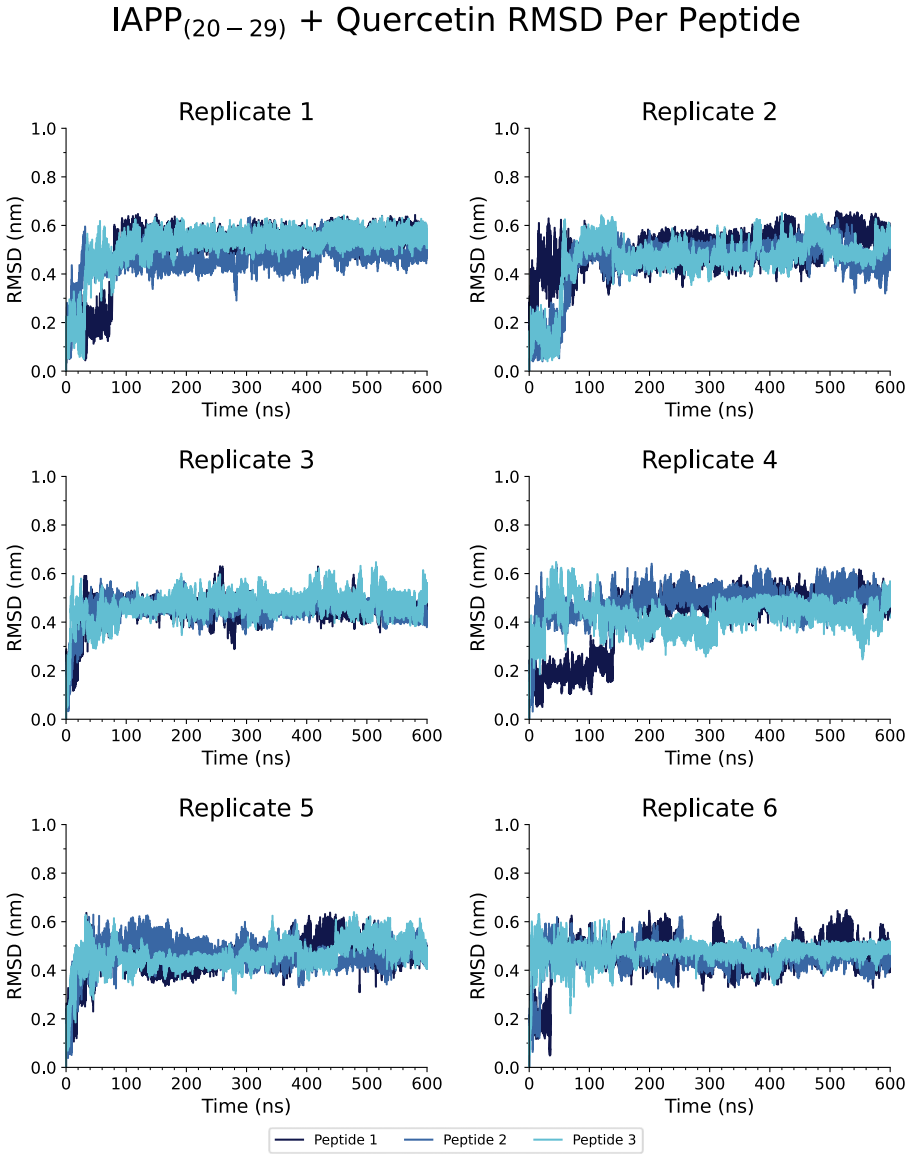

Figure S3: Root-mean-square deviation (RMSD) of $IAPP_{(20-29)}$ backbone atoms per peptide in the presence of quercetin. RMSD of the trimer is calculated per peptide over time with starting positions as reference. Calculations performed for individual peptides, with peptide 1 shown as dark blue, peptide 2 shown as medium blue, and peptide 3 shown as light blue.

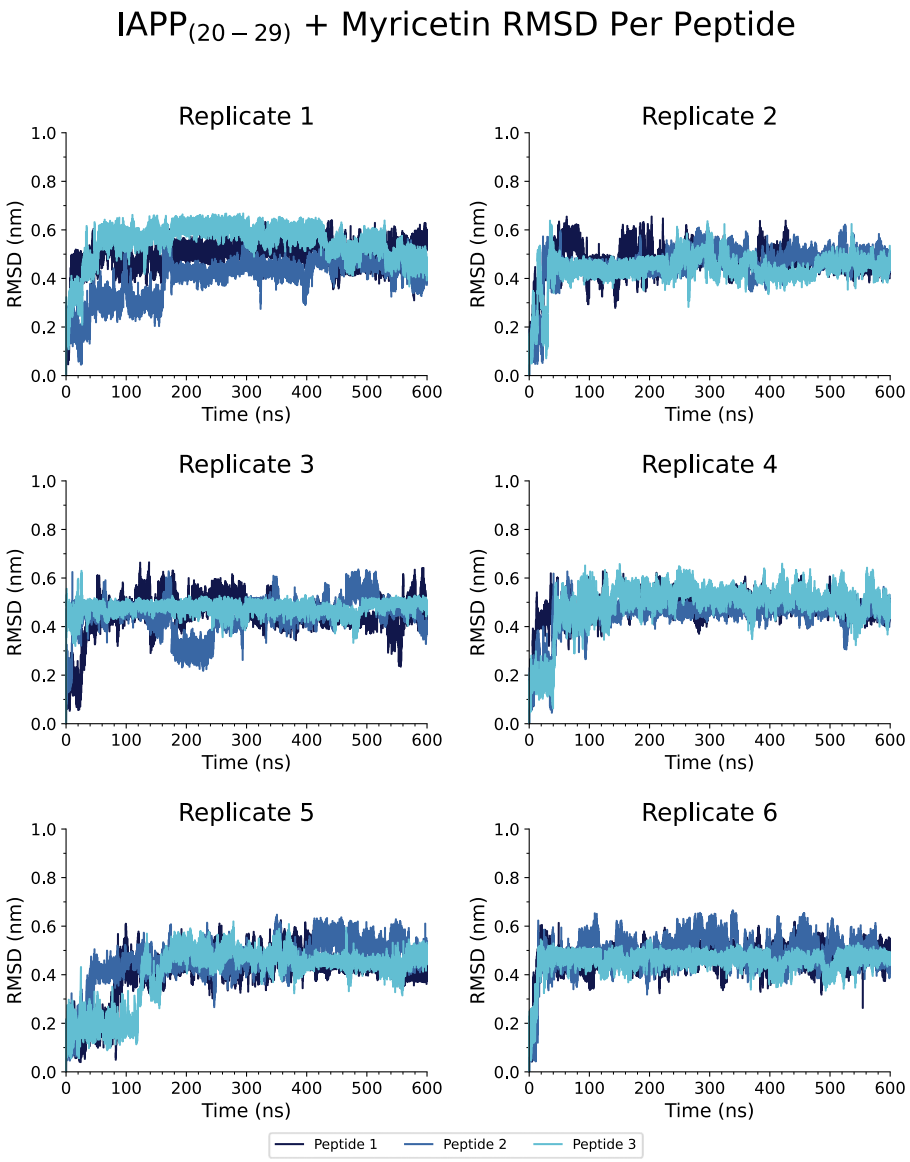

Figure S4: Root-mean-square deviation (RMSD) of $IAPP_{(20-29)}$ backbone atoms per peptide in the presence of myricetin. RMSD of the trimer is calculated per peptide over time with starting positions as reference. Calculations performed for individual peptides, with peptide 1 shown as dark blue, peptide 2 shown as medium blue, and peptide 3 shown as light blue.

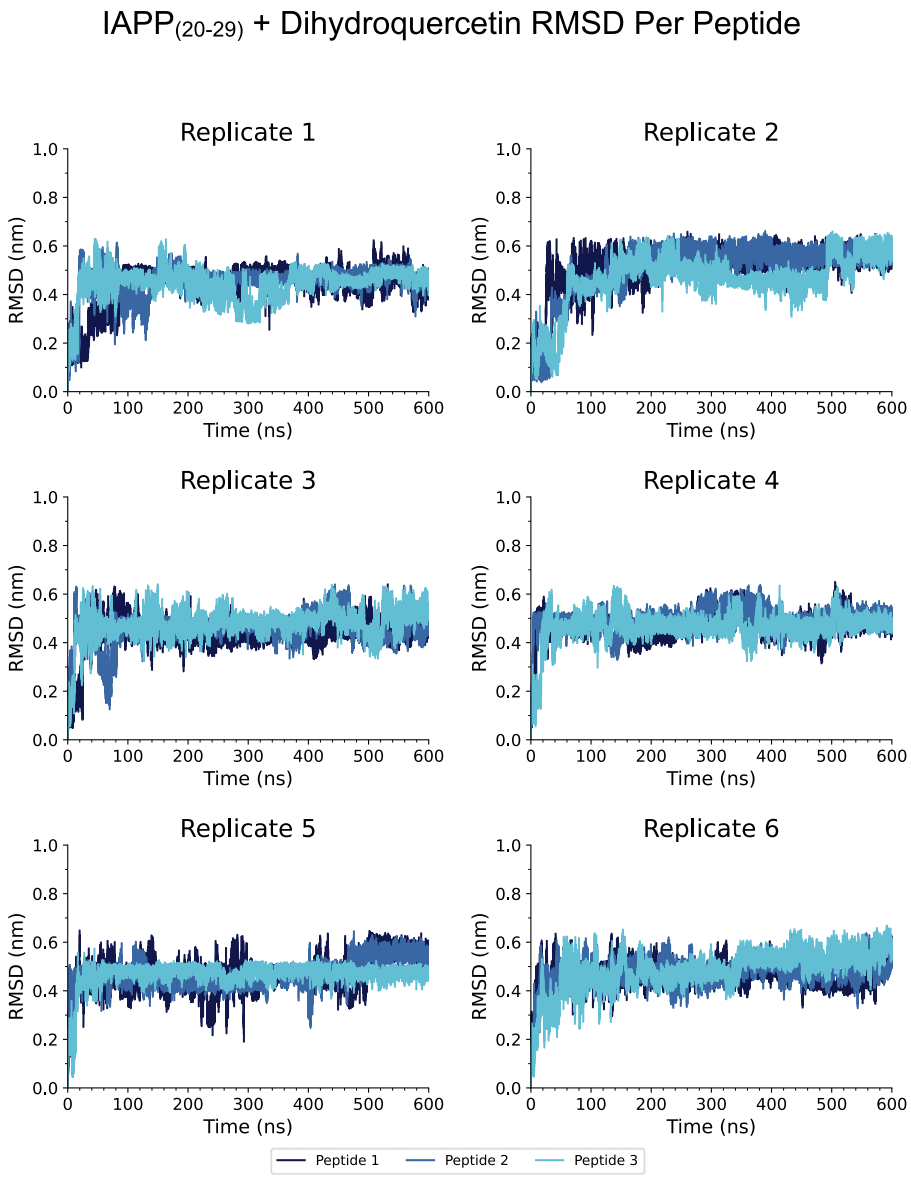

Figure S5: Root-mean-square deviation (RMSD) of $IAPP_{(20-29)}$ backbone atoms per peptide in the presence of dihydroquercetin. RMSD of the trimer is calculated per peptide over time with starting positions as reference. Calculations performed for individual peptides, with peptide 1 shown as dark blue, peptide 2 shown as medium blue, and peptide 3 shown as light blue.

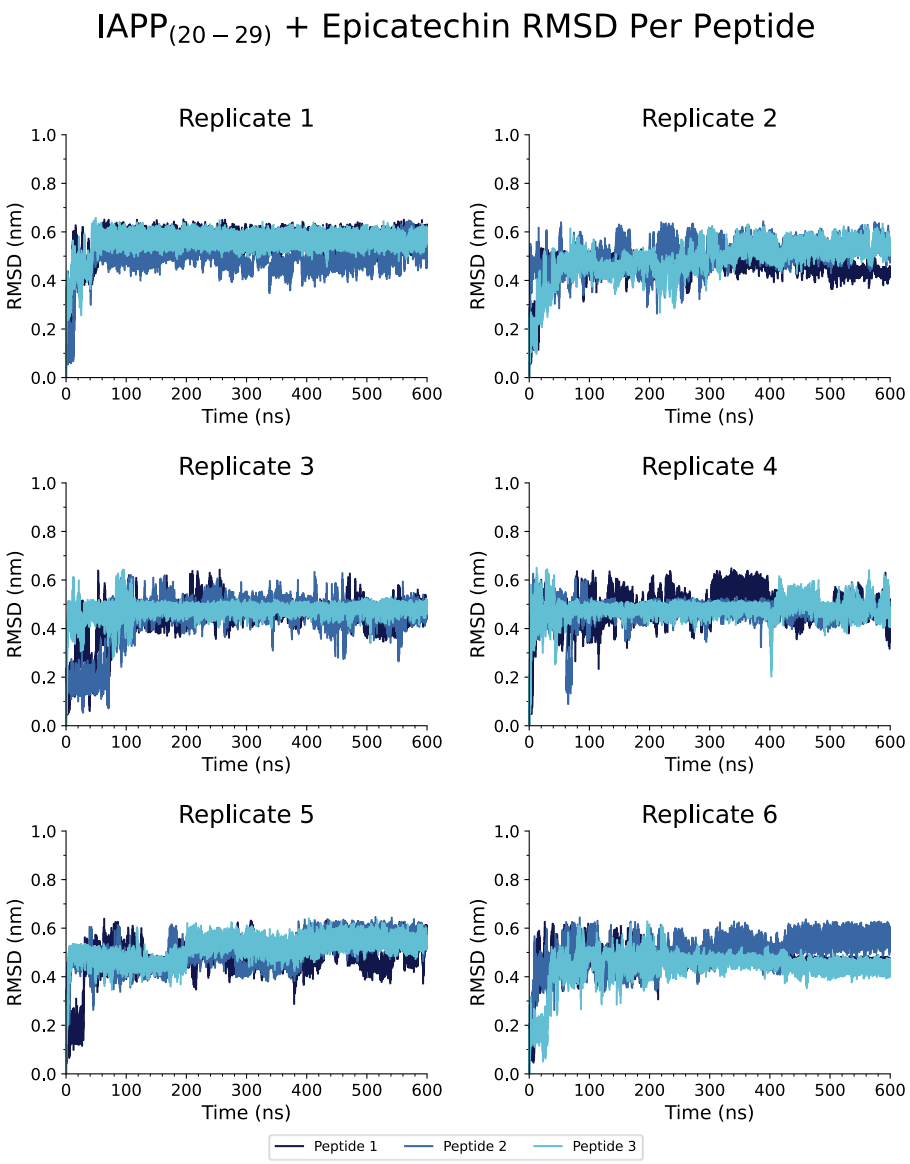

Figure S6: Root-mean-square deviation (RMSD) of $IAPP_{(20-29)}$ backbone atoms per peptide in the presence of epicatechin. RMSD of the trimer is calculated per peptide over time with starting positions as reference. Calculations performed for individual peptides, with peptide 1 shown as dark blue, peptide 2 shown as medium blue, and peptide 3 shown as light blue.

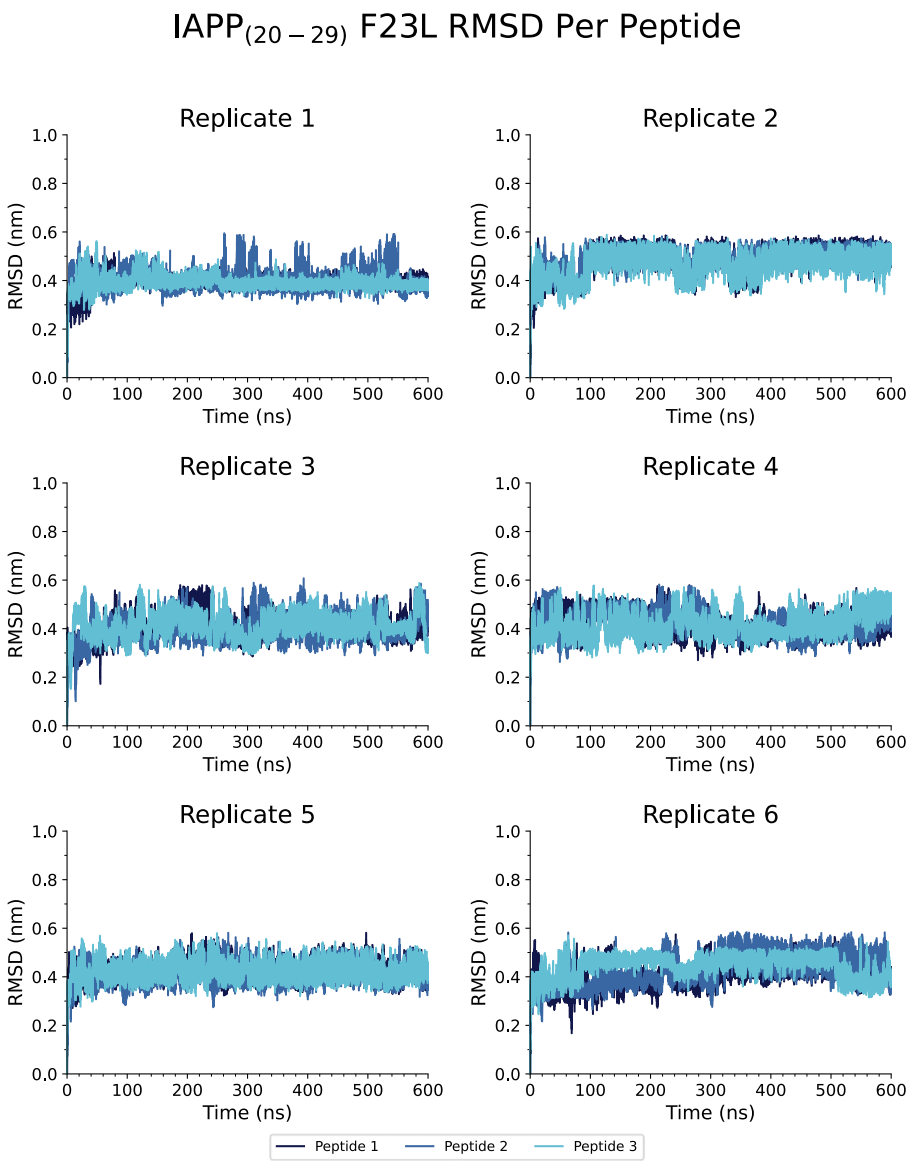

Figure S7: Root-mean-square deviation (RMSD) of $IAPP_{(20-29)}$ F23L backbone atoms per peptide. RMSD of the trimer is calculated per peptide over time with starting positions as reference. Calculations performed for individual peptides, with peptide 1 shown as dark blue, peptide 2 shown as medium blue, and peptide 3 shown as light blue.

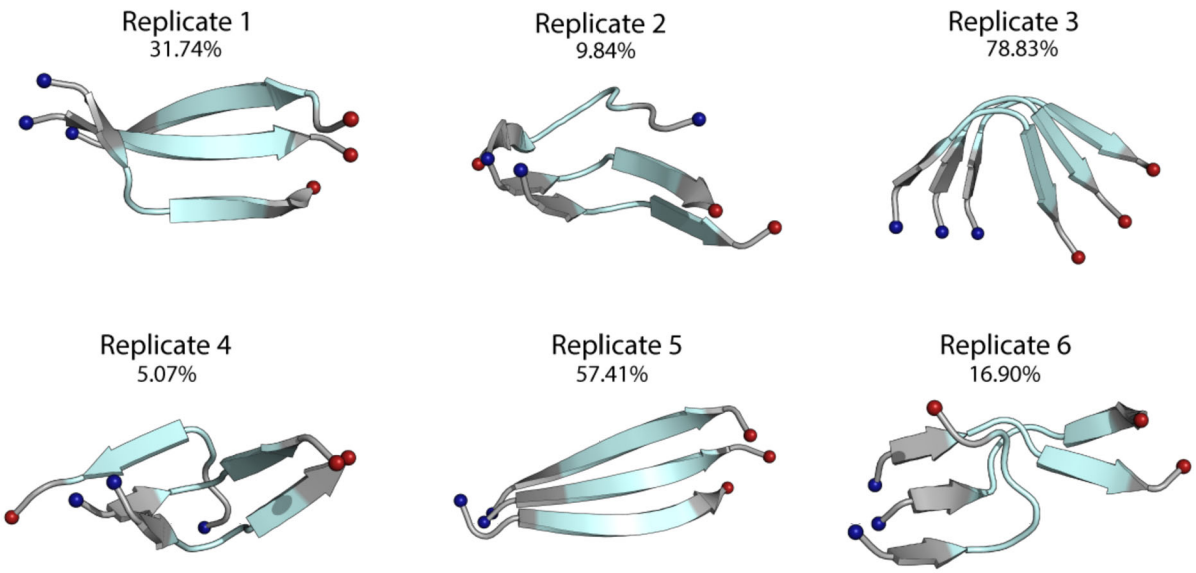

Figure S8: Representative structures from RMSD clustering of $IAPP_{(20-29)}$. Structures were obtained from backbone RMSD clustering over the last 200 ns of simulation. Peptides are shown as cartoon, with residues 23-27 (FGAIL) colored as teal. N- and C-termini are shown as spheres and colored as blue and red, respectively. Percentages indicate the percentage of frames the structure represents over the last 200 ns of simulation time.

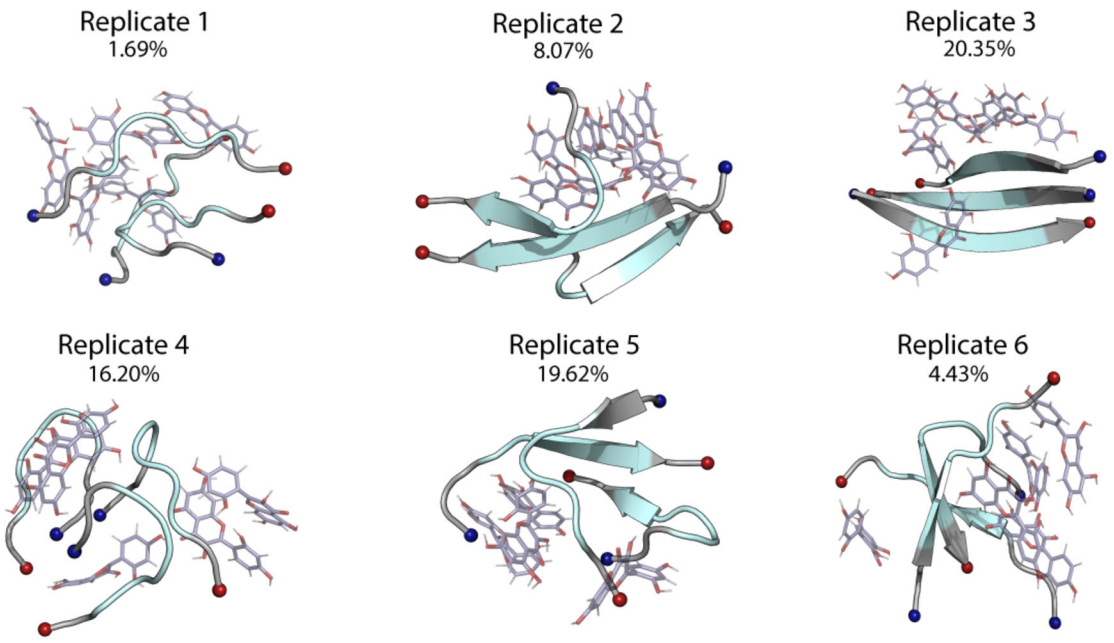

Figure S9: Representative structures from RMSD clustering of $IAPP_{(20-29)}$ in the presence of morin. Structures were obtained from backbone RMSD clustering over the last 200 ns of simulation. Peptides are shown as cartoon, with residues 23-27 (FGAIL) colored as teal. N- and C-termini are shown as spheres and colored as blue and red, respectively. Morin is shown as sticks, with oxygens colored red. Percentages indicate the percentage of frames the structure represents over the last 200 ns of simulation time.

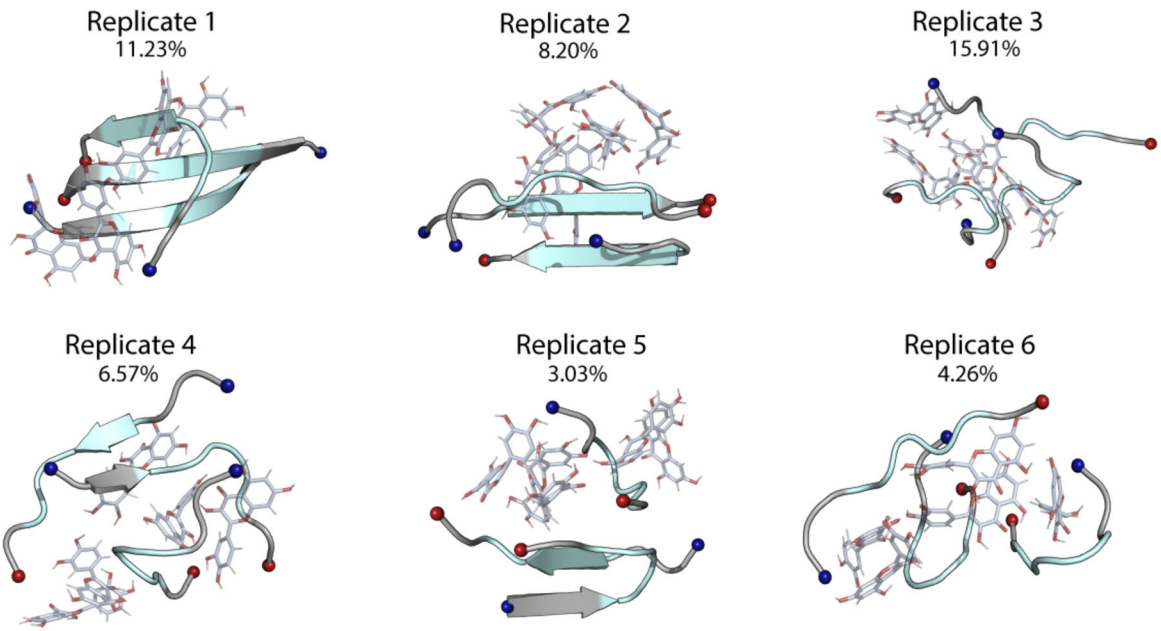

Figure S10: Representative structures from RMSD clustering of $IAPP_{(20-29)}$ in the presence of quercetin. Structures were obtained from backbone RMSD clustering over the last 200 ns of simulation. Peptides are shown as cartoon, with residues 23-27 (FGAIL) colored as teal. N- and C-termini are shown as spheres and colored as blue and red, respectively. Quercetin is shown as sticks, with oxygens colored red. Percentages indicate the percentage of frames the structure represents over the last 200 ns of simulation time.

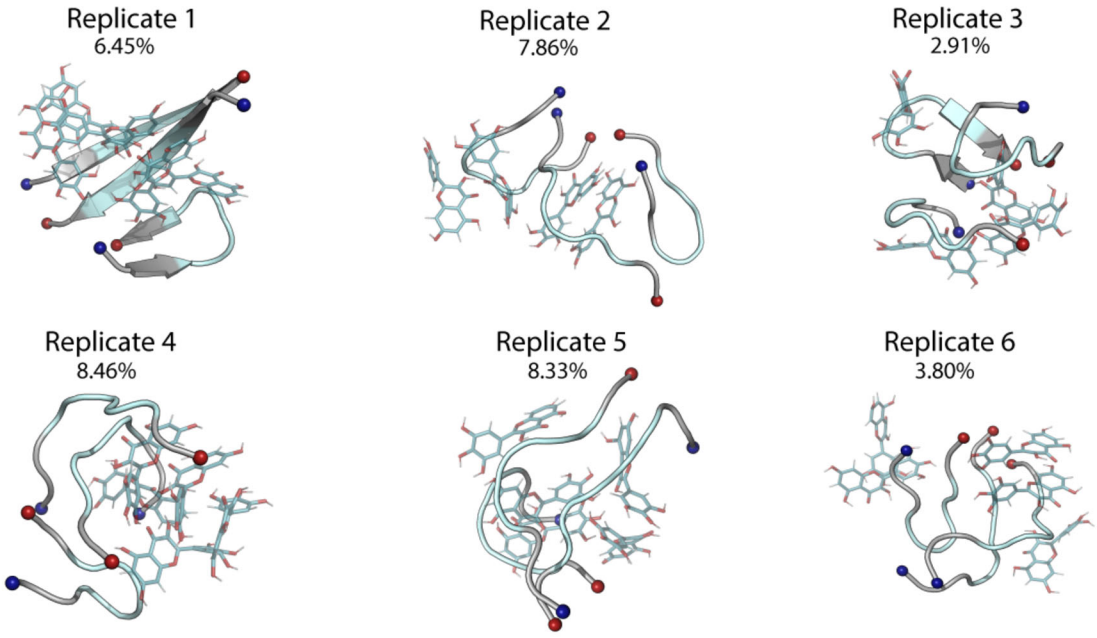

Figure S11: Representative structures from RMSD clustering of $IAPP_{(20-29)}$ in the presence of myricetin. Structures were obtained from backbone RMSD clustering over the last 200 ns of simulation. Peptides are shown as cartoon, with residues 23-27 (FGAIL) colored as teal. N- and C-termini are shown as spheres and colored as blue and red, respectively. Myricetin is shown as sticks, with oxygens colored red. Percentages indicate the percentage of frames the structure represents over the last 200 ns of simulation time.

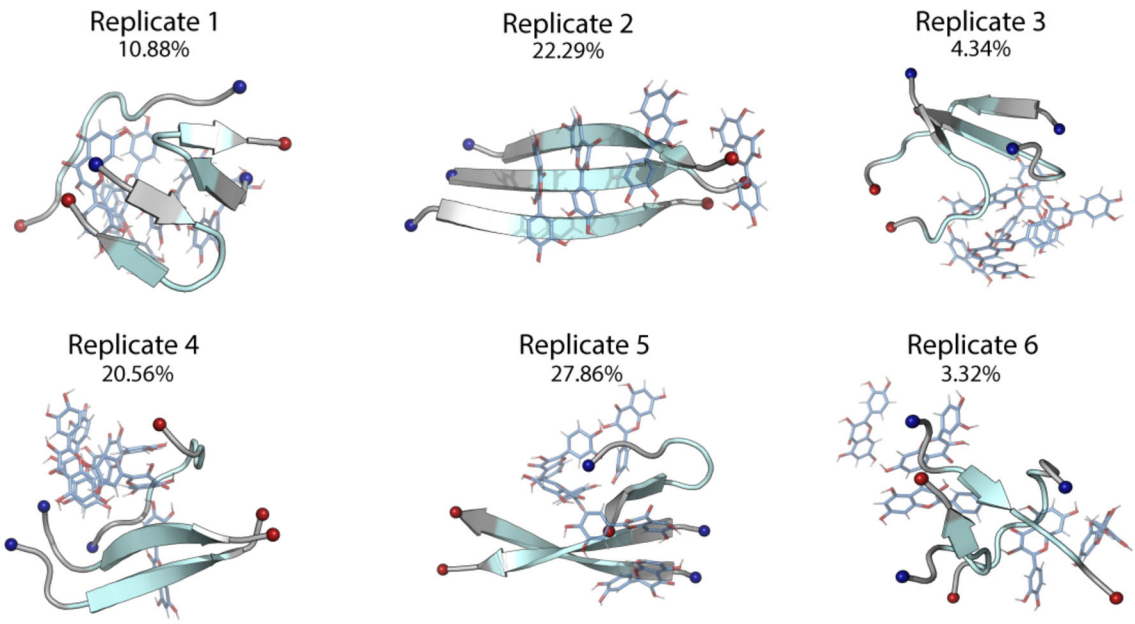

Figure S12: Representative structures from RMSD clustering of $IAPP_{(20-29)}$ in the presence of dihydroquercetin. Structures were obtained from backbone RMSD clustering over the last 200 ns of simulation. Peptides are shown as cartoon, with residues 23-27 (FGAIL) colored as teal. N- and C-termini are shown as spheres and colored as blue and red, respectively. Dihydroquercetin is shown as sticks, with oxygens colored red. Percentages indicate the percentage of frames the structure represents over the last 200 ns of simulation time.

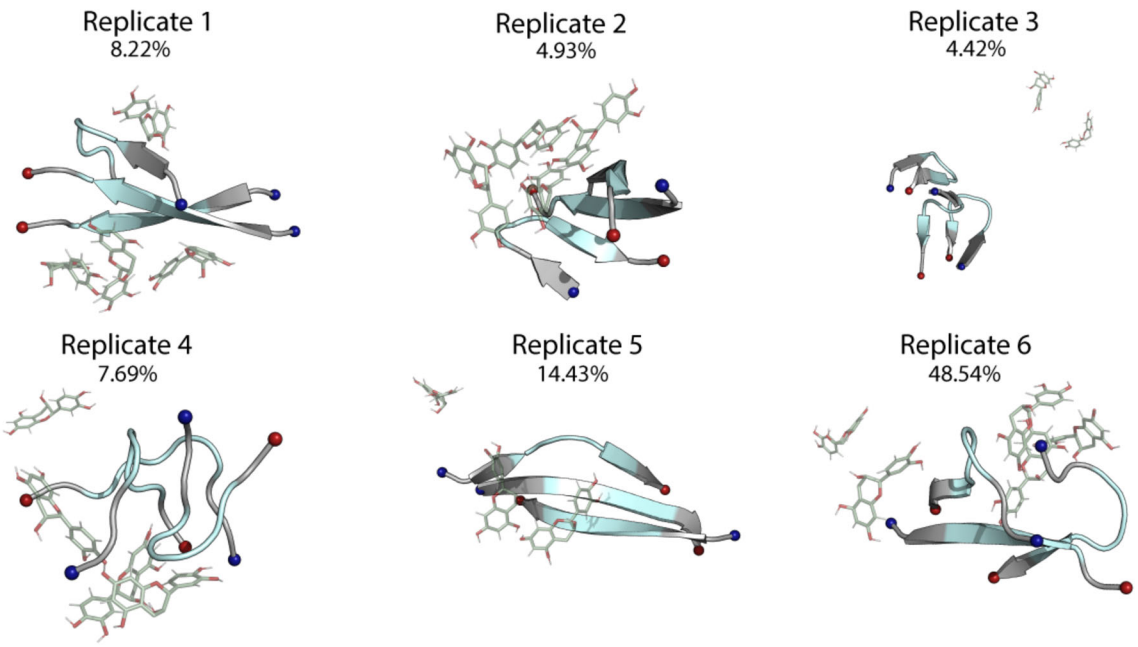

Figure S13: Representative structures from RMSD clustering of $IAPP_{(20-29)}$ in the presence of epicatechin. Structures were obtained from backbone RMSD clustering over the last 200 ns of simulation. Peptides are shown as cartoon, with residues 23-27 (FGAIL) colored as teal. N- and C-termini are shown as spheres and colored as blue and red, respectively. Epicatechin is shown as sticks, with oxygens colored red. Percentages indicate the percentage of frames the structure represents over the last 200 ns of simulation time.

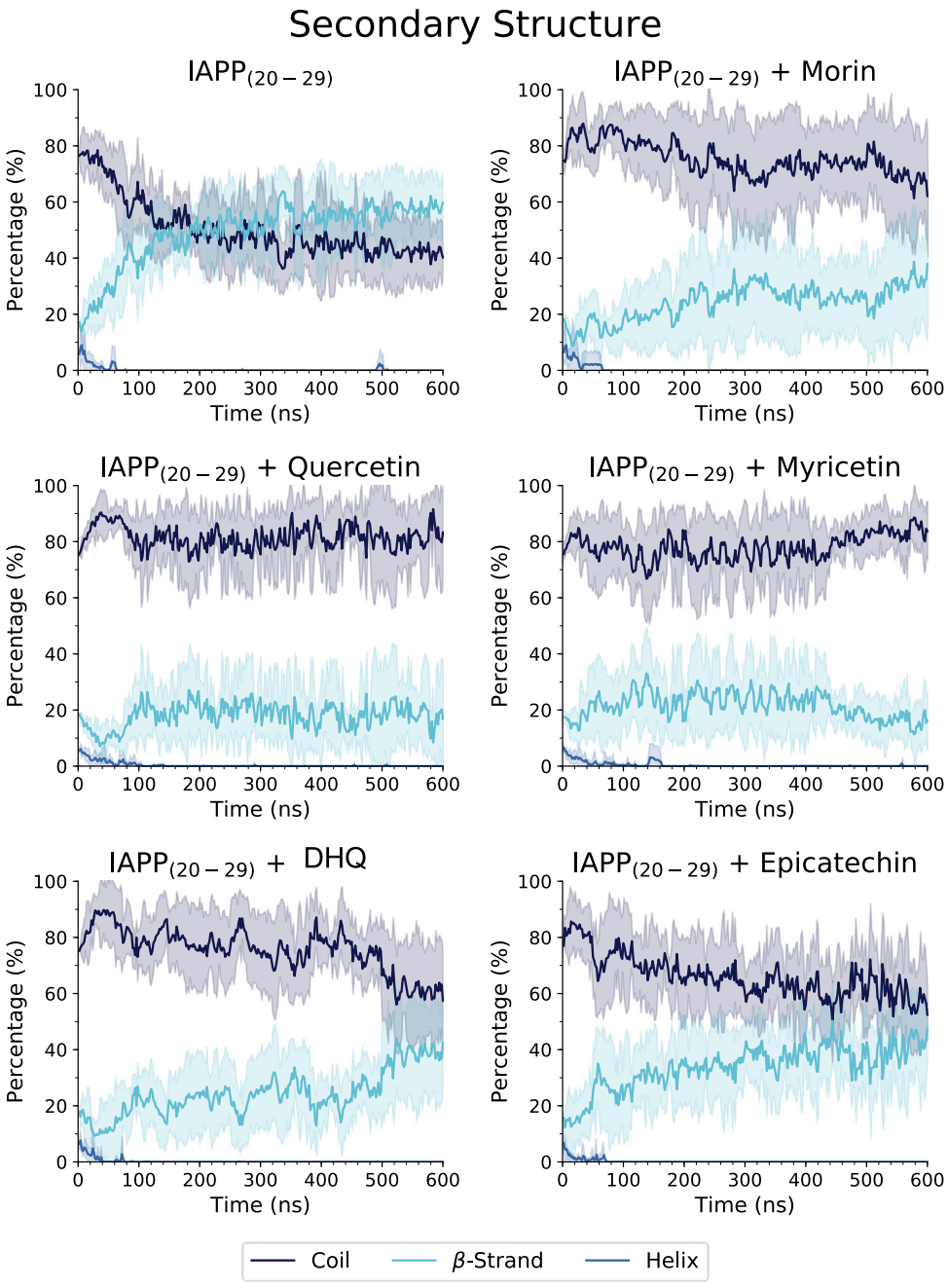

Figure S14: $IAPP_{(20-29)}$ secondary structure percentages over time. Random coil (dark blue), β-strand (light blue), and a-helix (medium blue) percentages were assigned using the DSSP algorithm. Plots represent the average over all replicates. Percentages were block-averaged every 10 ps.

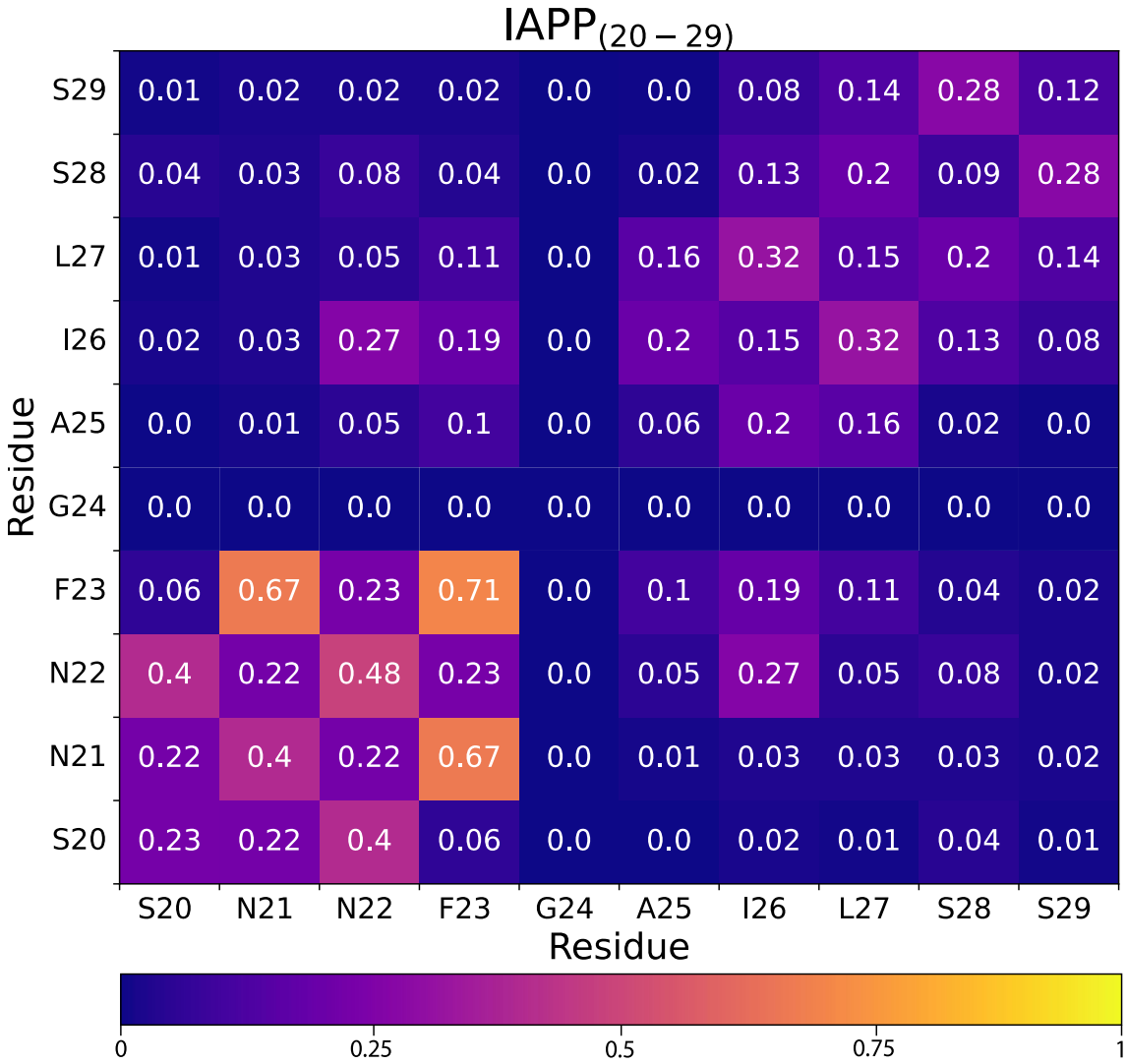

Figure S15: Interaction frequency (probability) maps between $IAPP_{(20-29)}$ sidechains. Frequencies represent the average across all peptides and all replicates. Frequency was calculated by taking the average number of sidechain-sidechain contacts within 0.6 nm over the last 200 ns of simulation divided by the number of interactors (sum of atoms between both residue sidechains).

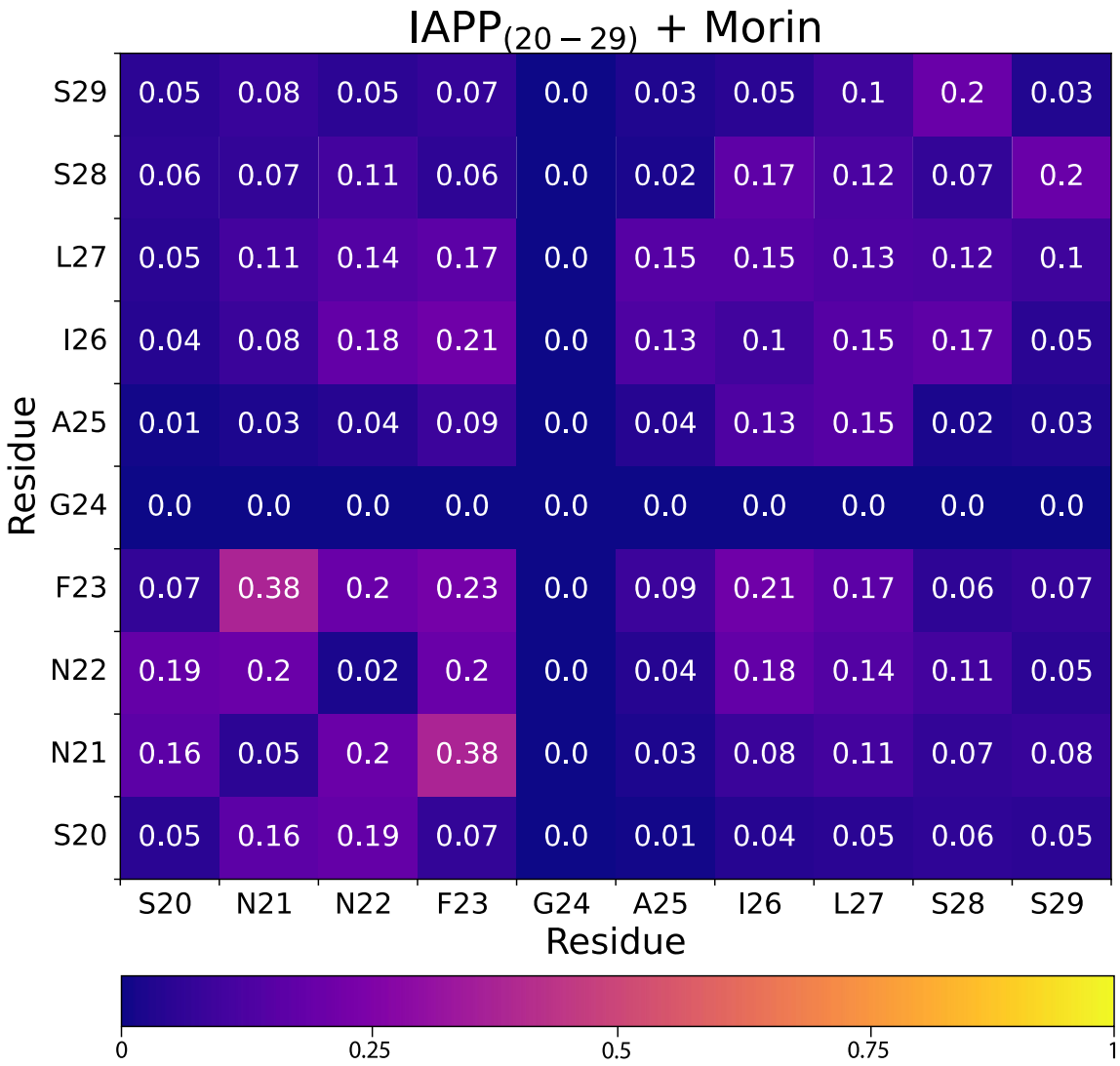

Figure S15: Interaction frequency (probability) maps between $IAPP_{(20-29)}$ sidechains. Frequencies represent the average across all peptides and all replicates. Frequency was calculated by taking the average number of sidechain-sidechain contacts within 0.6 nm over the last 200 ns of simulation divided by the number of interactors (sum of atoms between both residue sidechains).

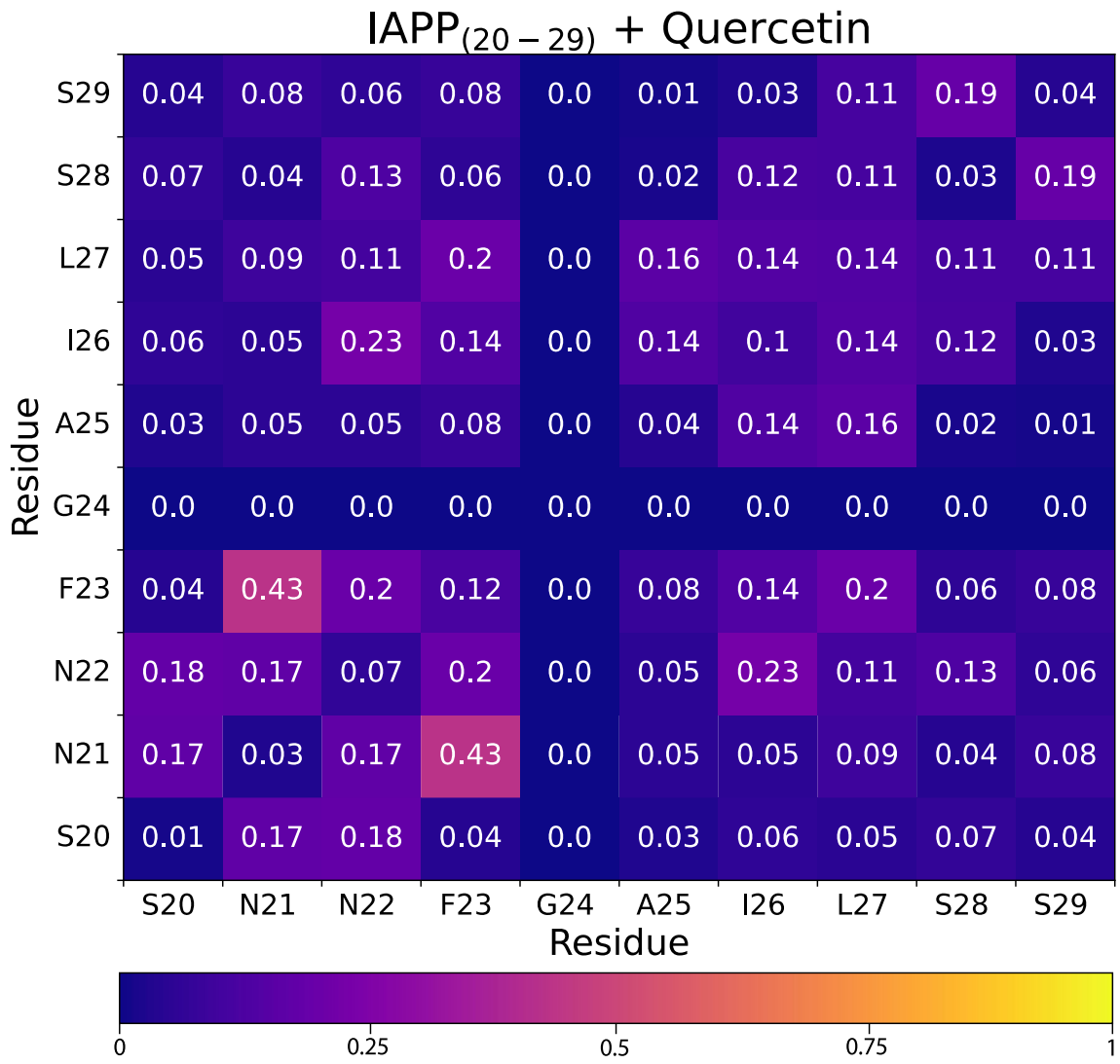

Figure S17: Interaction frequency (probability) maps between IAPP$_{(20-29)}$ sidechains in the presence of quercetin. Frequencies represent the average across all peptides and all replicates. Frequency was calculated by taking the average number of sidechain-sidechain contacts within 0.6 nm over the last 200 ns of simulation divided by the number of interactors (sum of atoms between both residue sidechains).

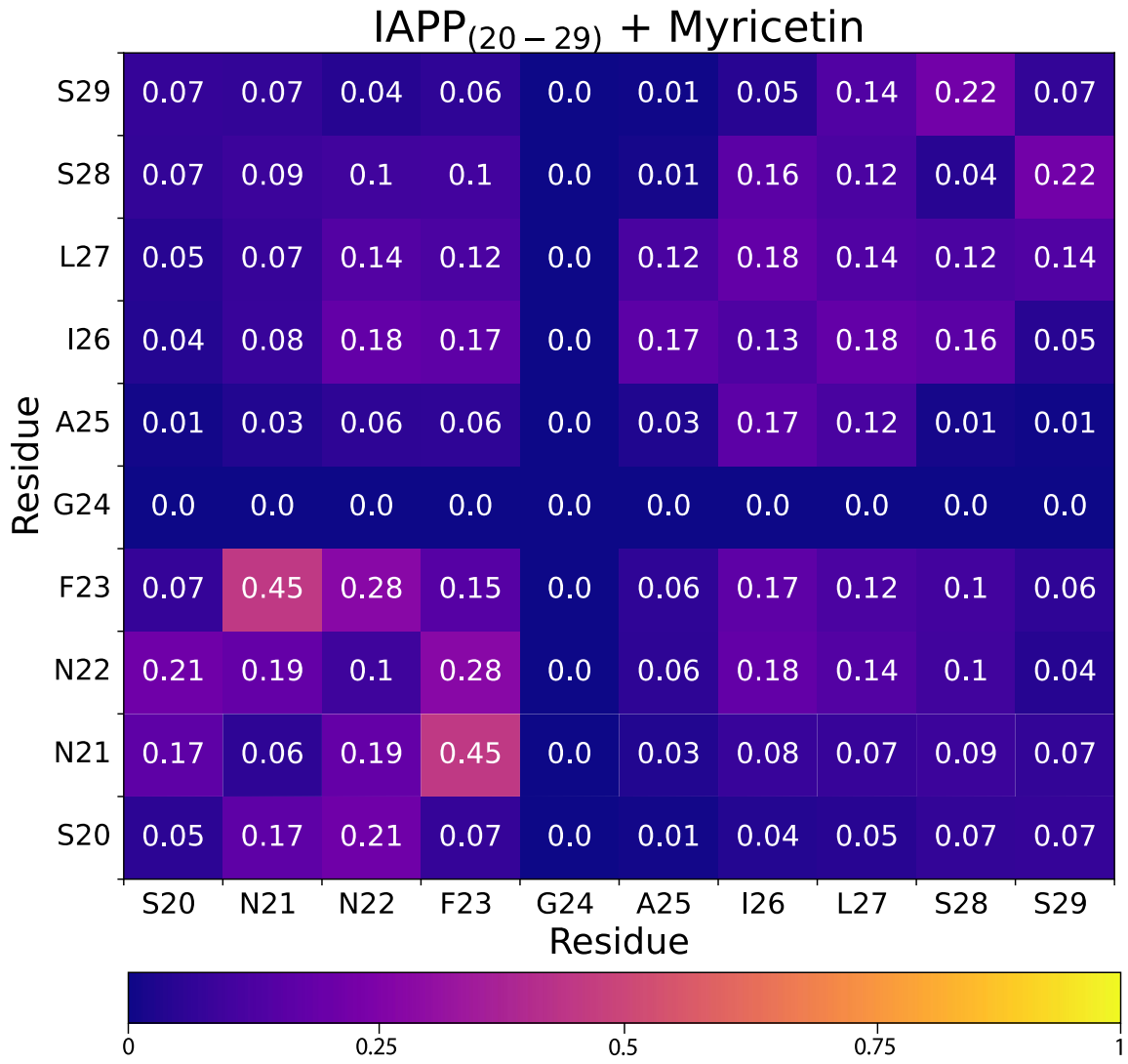

Figure S18: Interaction frequency (probability) maps between $IAPP_{(20-29)}$ sidechains in the presence of myricetin. Frequencies represent the average across all peptides and all replicates. Frequency was calculated by taking the average number of sidechain-sidechain contacts within 0.6 nm over the last 200 ns of simulation divided by the number of interactors (sum of atoms between both residue sidechains).

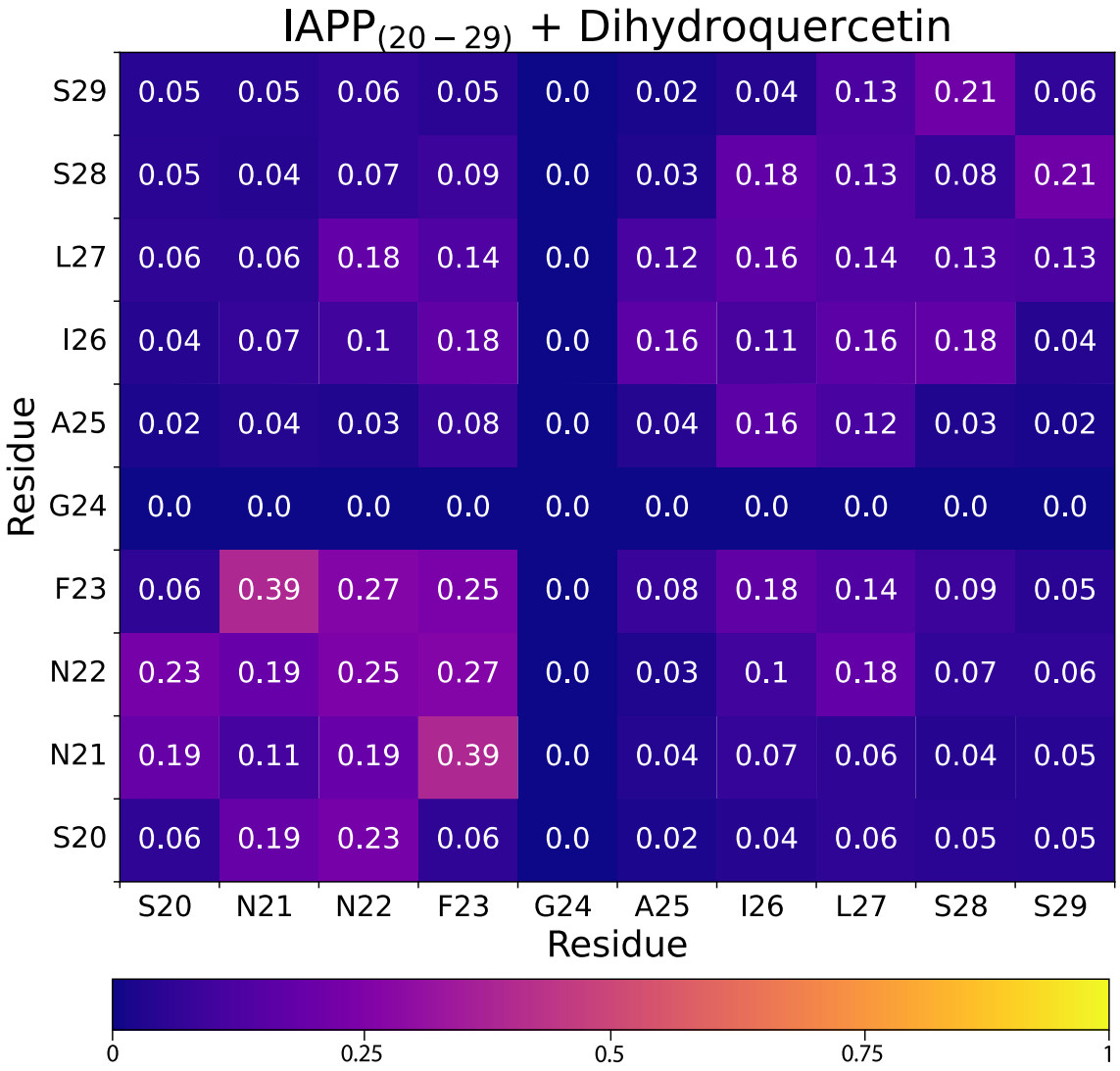

Figure S19: Interaction frequency (probability) maps between $IAPP_{(20-29)}$ sidechains in the presence of dihydroquercetin. Frequencies represent the average across all peptides and all replicates. Frequency was calculated by taking the average number of sidechain-sidechain contacts within 0.6 nm over the last 200 ns of simulation divided by the number of interactors (sum of atoms between both residue sidechains).

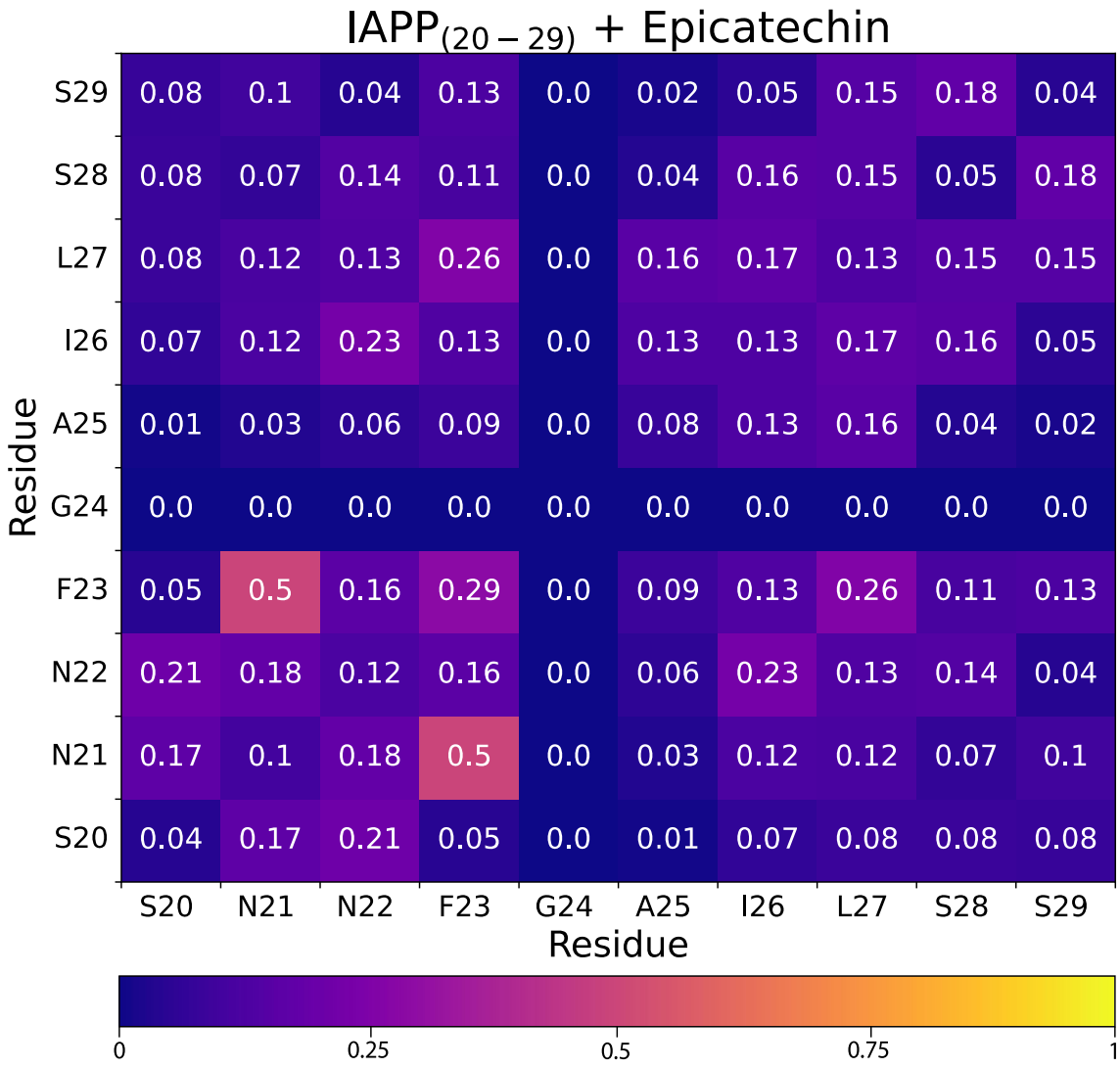

Figure S21: Interaction frequency (probability) maps between $IAPP_{(20-29)}$ sidechains in the presence of epicatechin. Frequencies represent the average across all peptides and all replicates. Frequency was calculated by taking the average number of sidechain-sidechain contacts within 0.6 nm over the last 200 ns of simulation divided by the number of interactors (sum of atoms between both residue sidechains).

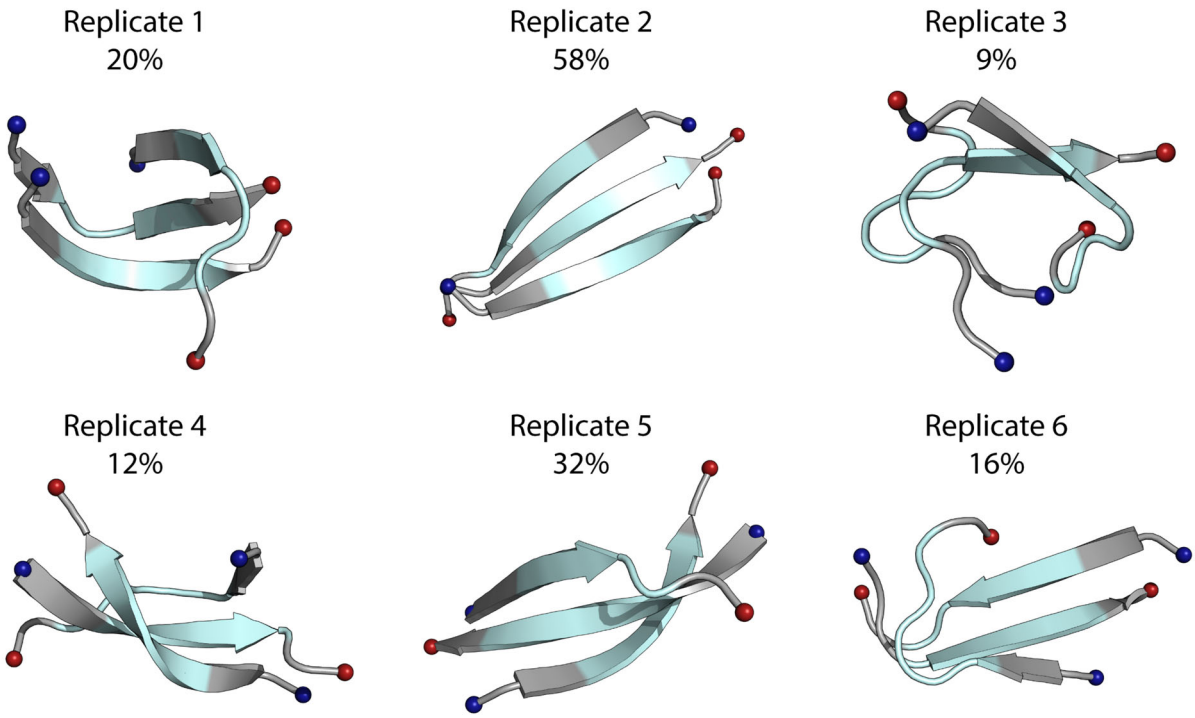

Figure S20 Representative structures from RMSD clustering of $IAPP_{(20-29)}$ mutant Phe23LEU (F23L). Structures were obtained from backbone RMSD clustering over the last 200 ns of simulation. Peptides are shown as cartoon, with residues 23-27 (FGAIL) colored as teal. N- and C-termini are shown as spheres and colored as blue and red, respectively. Percentages indicate the percentage of frames the structure represents over the last 200 ns of simulation time.

Table S1. R^2 values from linear regression to assess correlation between sidechain-sidechain contact frequencies and β-strand structure percentage across systems ($IAPP_{(20-29)}$, $IAPP_{(20-29)}$ + morin, $IAPP_{(20-29)}$ + quercetin, $IAPP_{(20-29)}$ + myricetin, $IAPP_{(20-29)}$ + dihydroquercetin, $IAPP_{(20-29)}$ + epicatechin). Frequencies and β-strand percentages were averages across all replicates and peptides.

Sidechain-Sidechain Contact	R^2
SER20-SER20	0.74
ASN21-ASN21	0.84
ASN22-ASN22	0.70
Phe23-Phe23	0.91
GLY24-GLY24	0
ALA25-ALA25	0.41
ILE26-ILE26	0.56
LEU27-LEU27	0.20
SER28-SER28	0.54
SER29-SER29	0.52

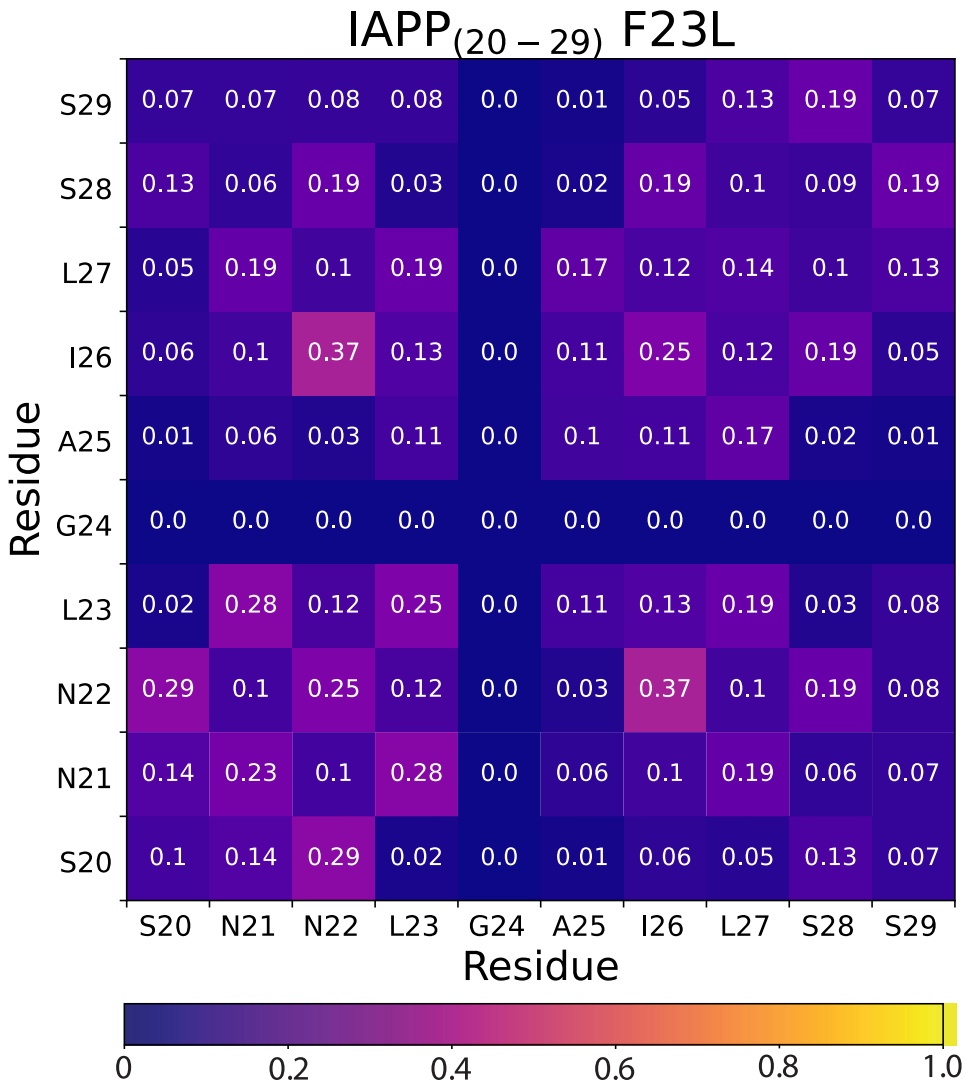

Figure S22: Interaction frequency (probability) maps between $IAPP_{(20-29)}$ mutant F23L sidechains. Frequencies represent the average across all peptides and all replicates. Frequency was calculated by taking the average number of sidechain-sidechain contacts within 0.6 nm over the last 200 ns of simulation divided by the number of interactors (sum of atoms between both residue sidechains).

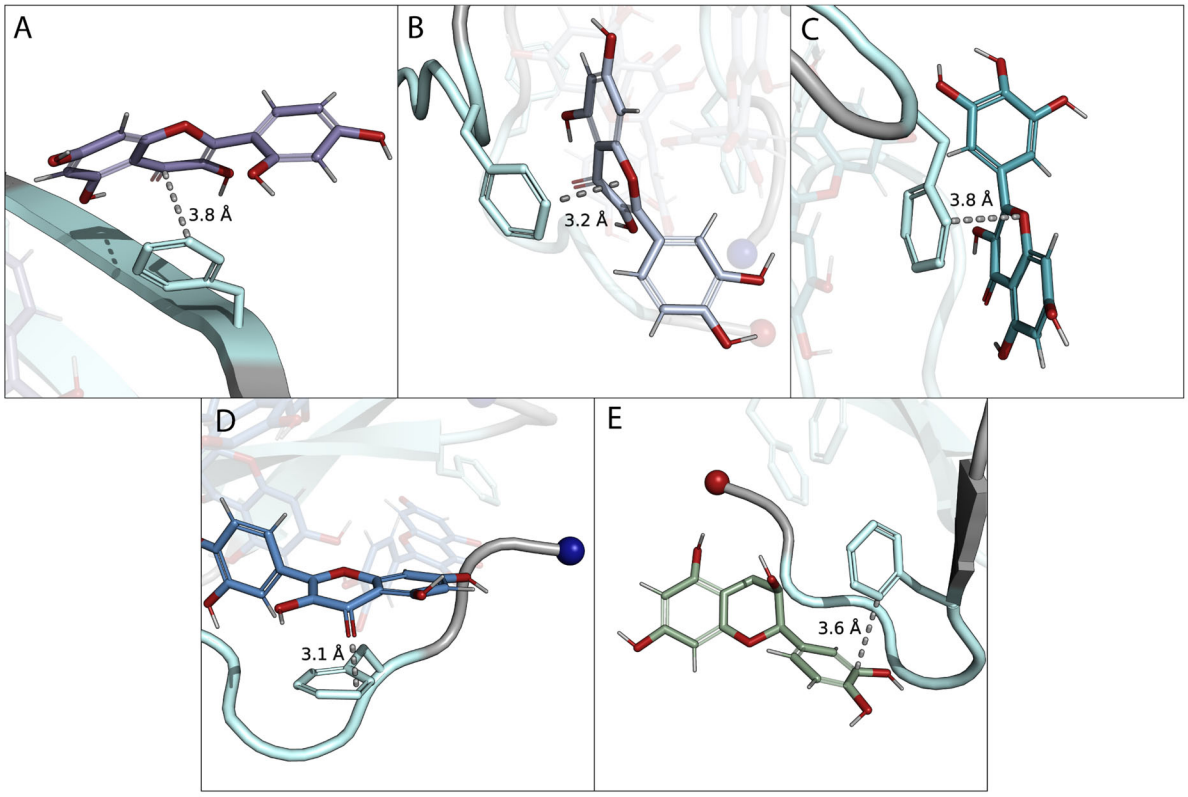

Figure S23: Example π interactions between Phe23 residues and **(A)** morin, **(B)** quercetin, **(C)** myricetin, **(D)** dihydroquercetin, **(F)** epicatechin. Interactions were chosen for visualization based on highest frequency π interactions. Distances are marked in Angstroms. Peptides are shown as cartoon, with residues 23-27 (FGAIL) colored teal. Phe23 residues are shown as teal sticks. Small molecules are shown as sticks, with oxygens colored red, and hydrogens shown as white sticks. Peptide N- and C-termini are colored blue and red, respectively, and shown as spheres.

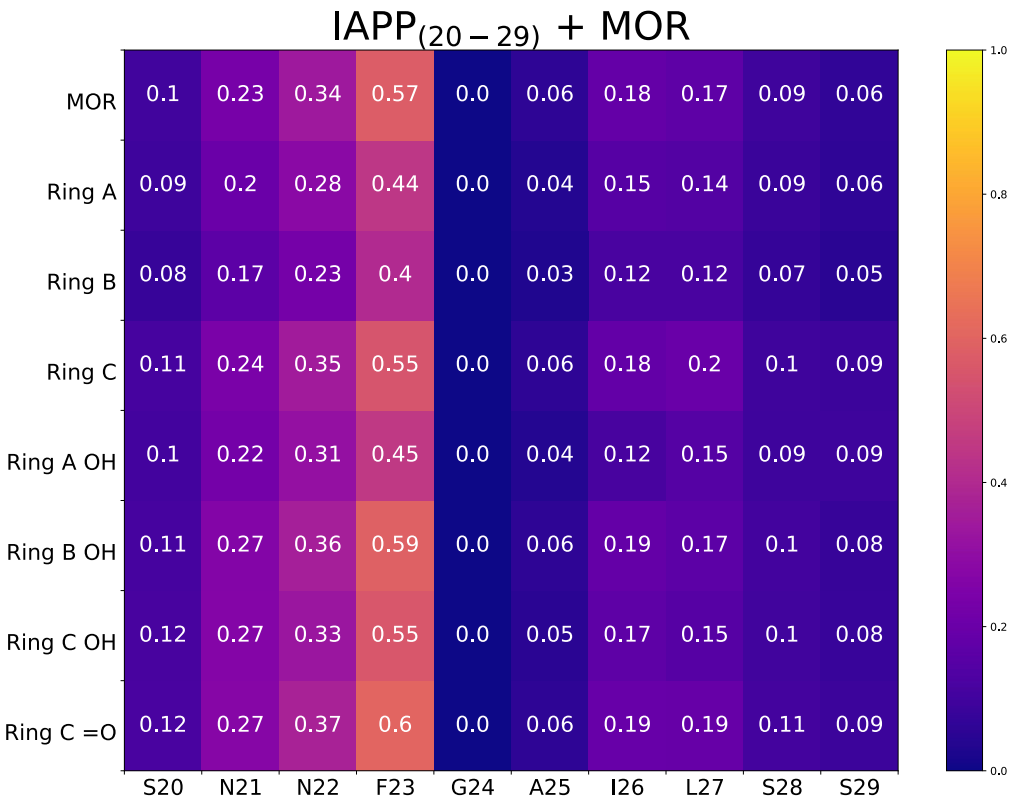

Figure S24: Interaction frequency (probability) maps between $IAPP_{(20-29)}$ sidechains and morin (MOR) by functional group. MOR takes into account the entire small molecule. Ring A, Ring B, and Ring C take into account interactions with ring A, B, and C carbons. Ring A OH, Ring B OH, and Ring C OH take into account hydroxyl groups (oxygen and hydrogen) on their respective rings. Ring C =O takes into account the C-ring carbonyl oxygen only. Frequencies represent the average across all peptides, small molecules, and all replicates. Frequency was calculated by taking the average number of sidechain-functional group contacts within 0.6 nm over the last 200 ns of simulation divided by the number of interactors (sum of atoms between functional group and sidechain).

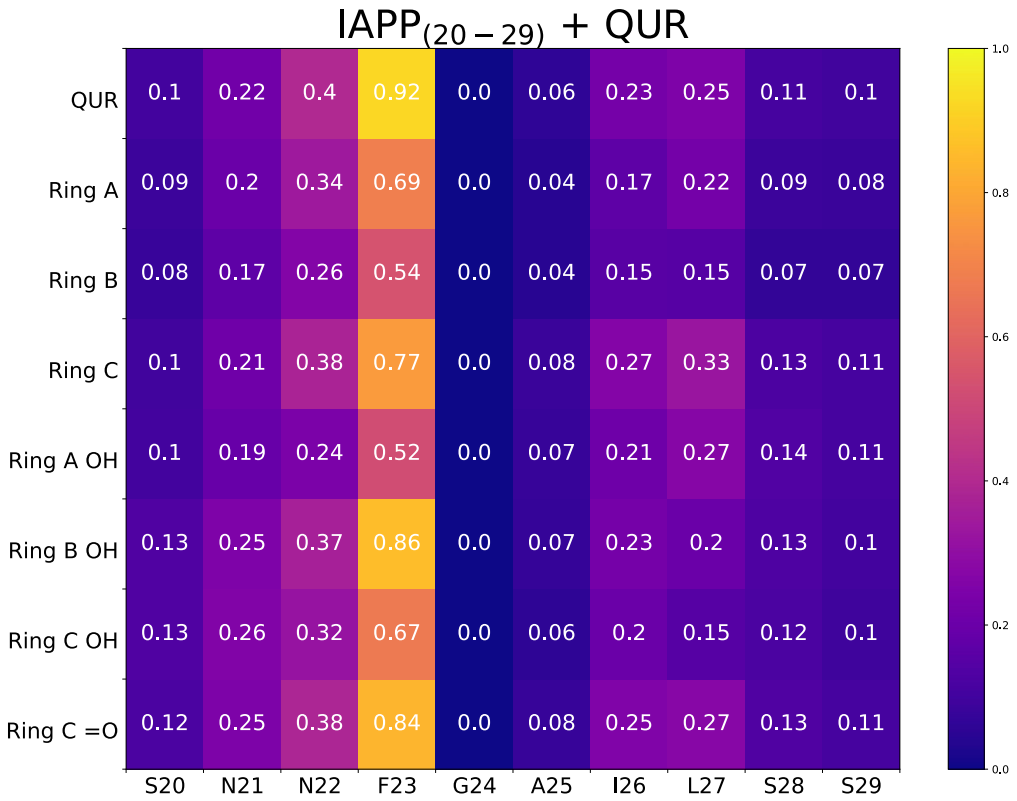

Figure S25: Interaction frequency (probability) maps between $IAPP_{(20-29)}$ sidechains and quercetin (QUR) by functional group. QUR takes into account the entire small molecule. Ring A, Ring B, and Ring C take into account interactions with ring A, B, and C carbons. Ring A OH, Ring B OH, and Ring C OH take into account hydroxyl groups (oxygen and hydrogen) on their respective rings. Ring C =O takes into account the C-ring carbonyl oxygen only. Frequencies represent the average across all peptides, small molecules, and all replicates. Frequency was calculated by taking the average number of sidechain-functional group contacts within 0.6 nm over the last 200 ns of simulation divided by the number of interactors (sum of atoms between functional group and sidechain).

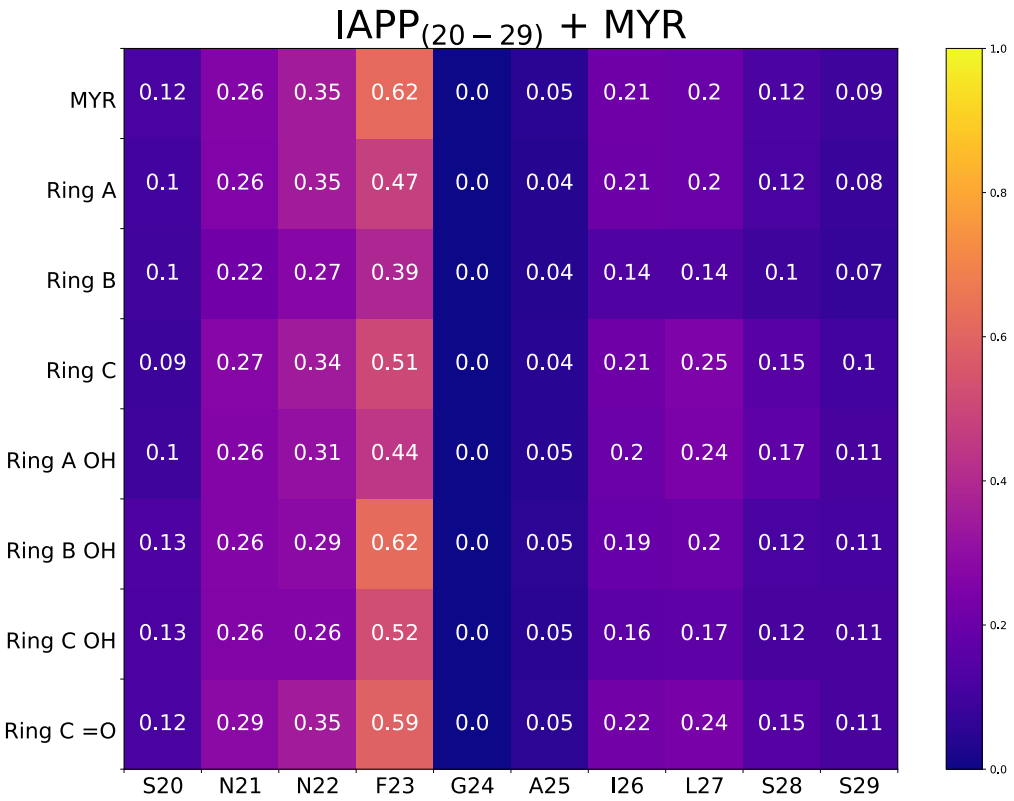

Figure S26: Interaction frequency (probability) maps between $IAPP_{(20-29)}$ sidechains and myricetin (MYR) by functional group. MYR takes into account the entire small molecule. Ring A, Ring B, and Ring C take into account interactions with ring A, B, and C carbons. Ring A OH, Ring B OH, and Ring C OH take into account hydroxyl groups (oxygen and hydrogen) on their respective rings. Ring C =O takes into account the C-ring carbonyl oxygen only. Frequencies represent the average across all peptides, small molecules, and all replicates. Frequency was calculated by taking the average number of sidechain-functional group contacts within 0.6 nm over the last 200 ns of simulation divided by the number of interactors (sum of atoms between functional group and sidechain).

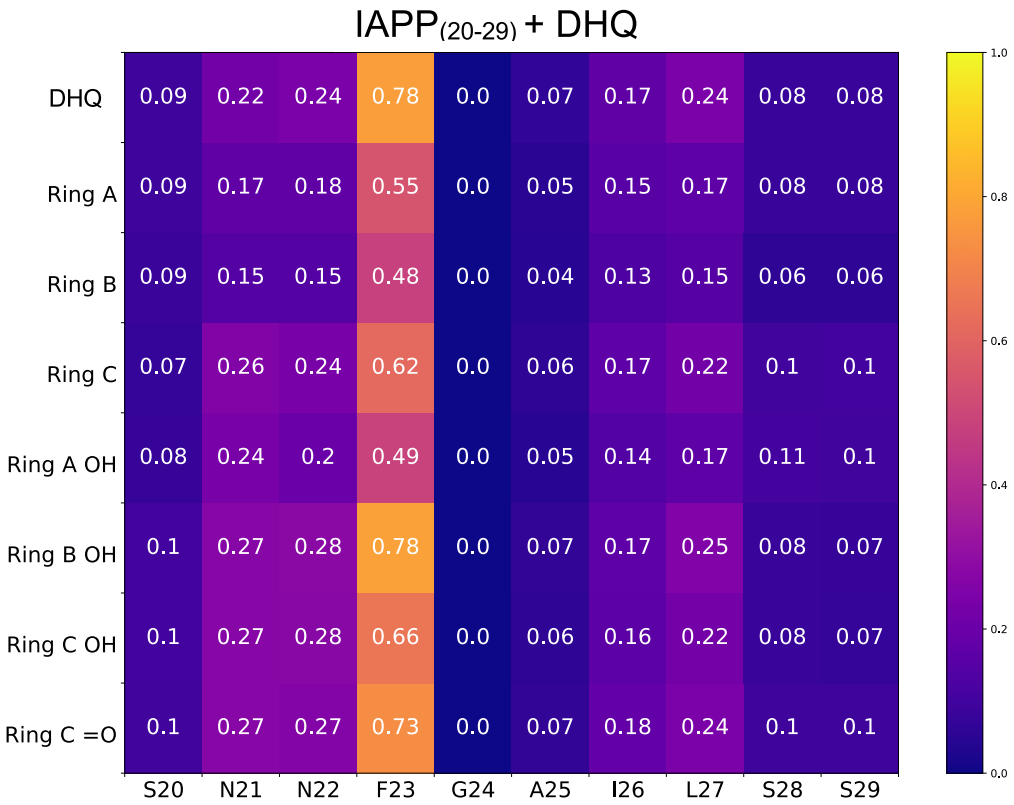

Figure S27: Interaction frequency (probability) maps between IAPP$_{(20-29)}$ sidechains and dihydroquercetin (DHQ*) by functional group. DHQ takes into account the entire small molecule. Ring A, Ring* B, and Ring C take into account interactions with ring A, B, and C carbons. Ring A OH, Ring B OH, and Ring C OH take into account hydroxyl groups (oxygen and hydrogen) on their respective rings. Ring C =O takes into account the C-ring carbonyl oxygen only. Frequencies represent the average across all peptides, small molecules, and all replicates. Frequency was calculated by taking the average number of sidechain-functional group contacts within 0.6 nm over the last 200 ns of simulation divided by the number of interactors (sum of atoms between functional group and sidechain).

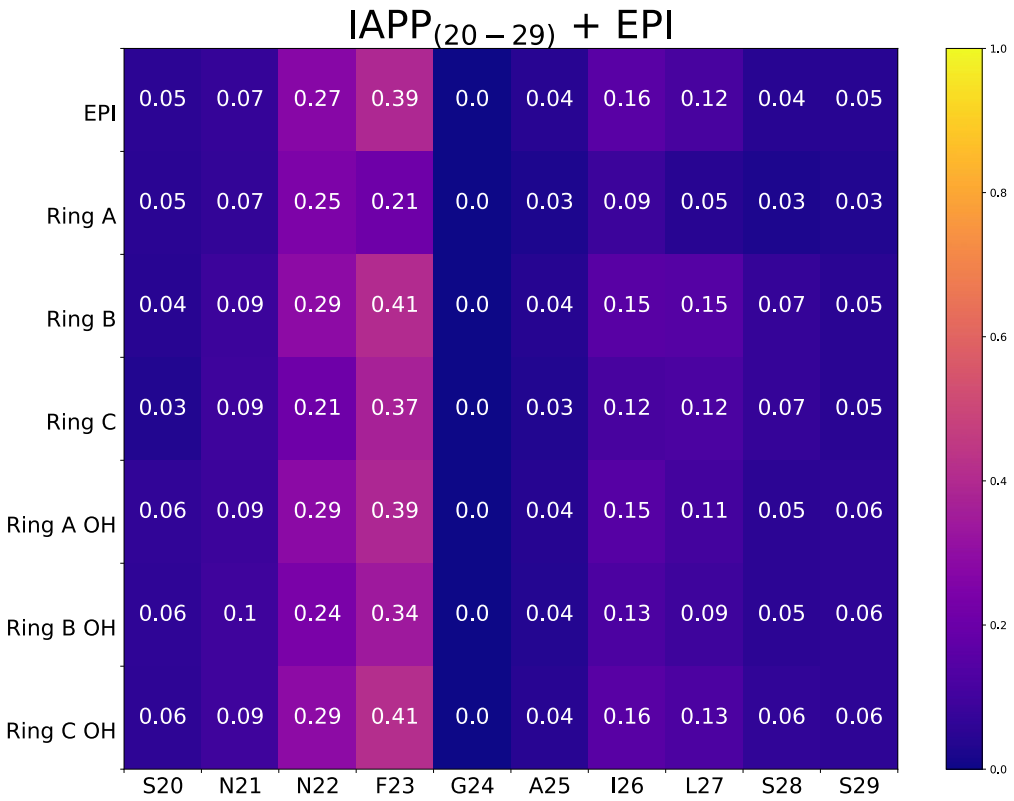

Figure S28: Interaction frequency (probability) maps between $IAPP_{(20-29)}$ sidechains and epicatechin (EPI) by functional group. EPI takes into account the entire small molecule. Ring A, Ring B, and Ring C take into account interactions with ring A, B, and C carbons. Ring A OH, Ring B OH, and Ring C OH take into account hydroxyl groups (oxygen and hydrogen) on their respective rings. Frequencies represent the average across all peptides, small molecules, and all replicates. Frequency was calculated by taking the average number of sidechain-functional group contacts within 0.6 nm over the last 200 ns of simulation divided by the number of interactors (sum of atoms between functional group and sidechain).

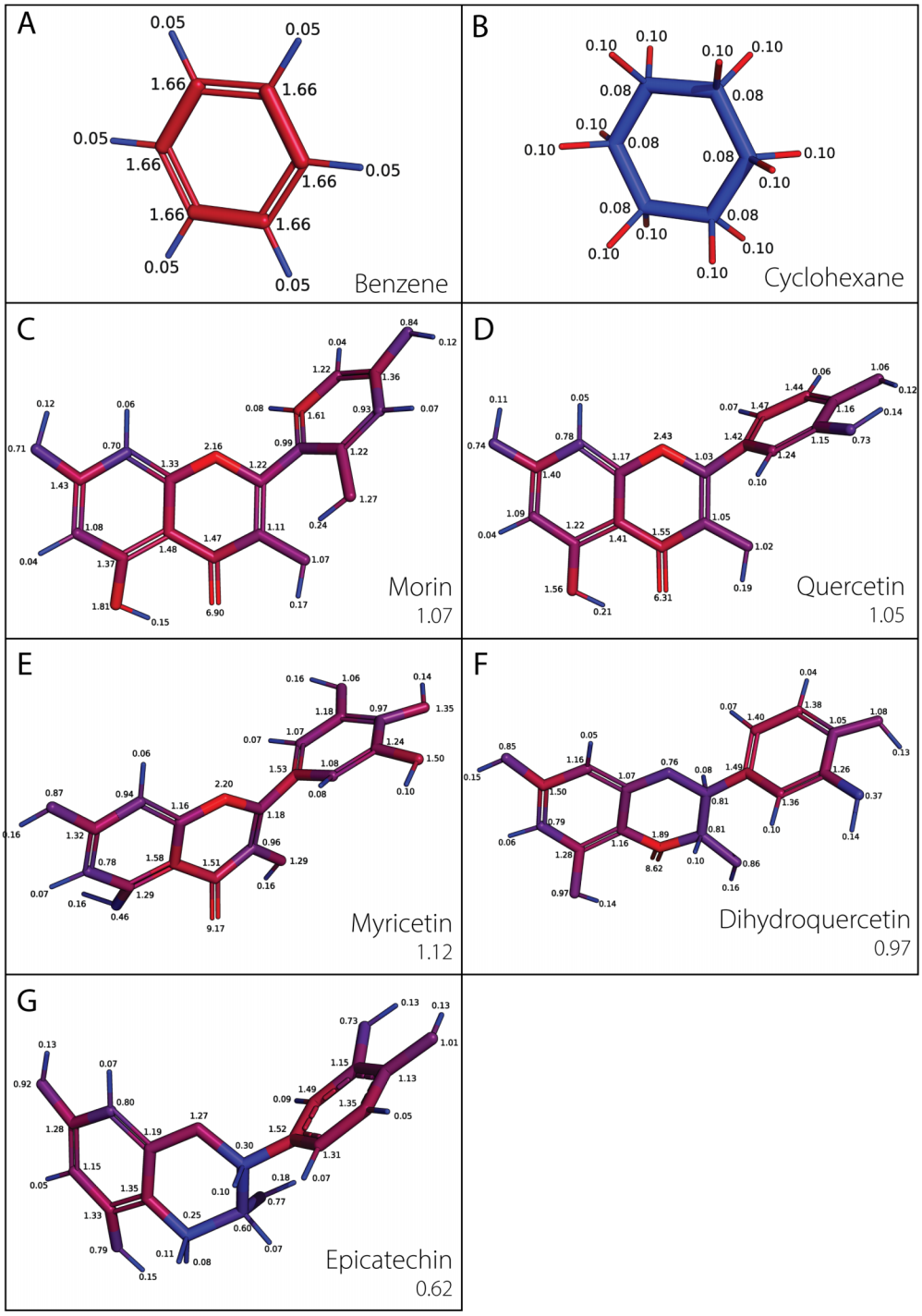

Figure S29: Anisotropy calculated per-atom for **(A)** benzene and **(B)** cyclohexane as references for aromatic and non-aromatic systems, respectively. Anisotropy was then calculated per-atom for **(C)** morin, **(D)** quercetin, **(E)** myricetin, **(F)** dihydroquercetin, and **(G)** epicatechin. Atoms are colored by anisotropy and labeled by their value. Numbers in the bottom-right corner represent the average anisotropy for the molecule. Epicatechin exhibits higher flexibility in the C-ring.

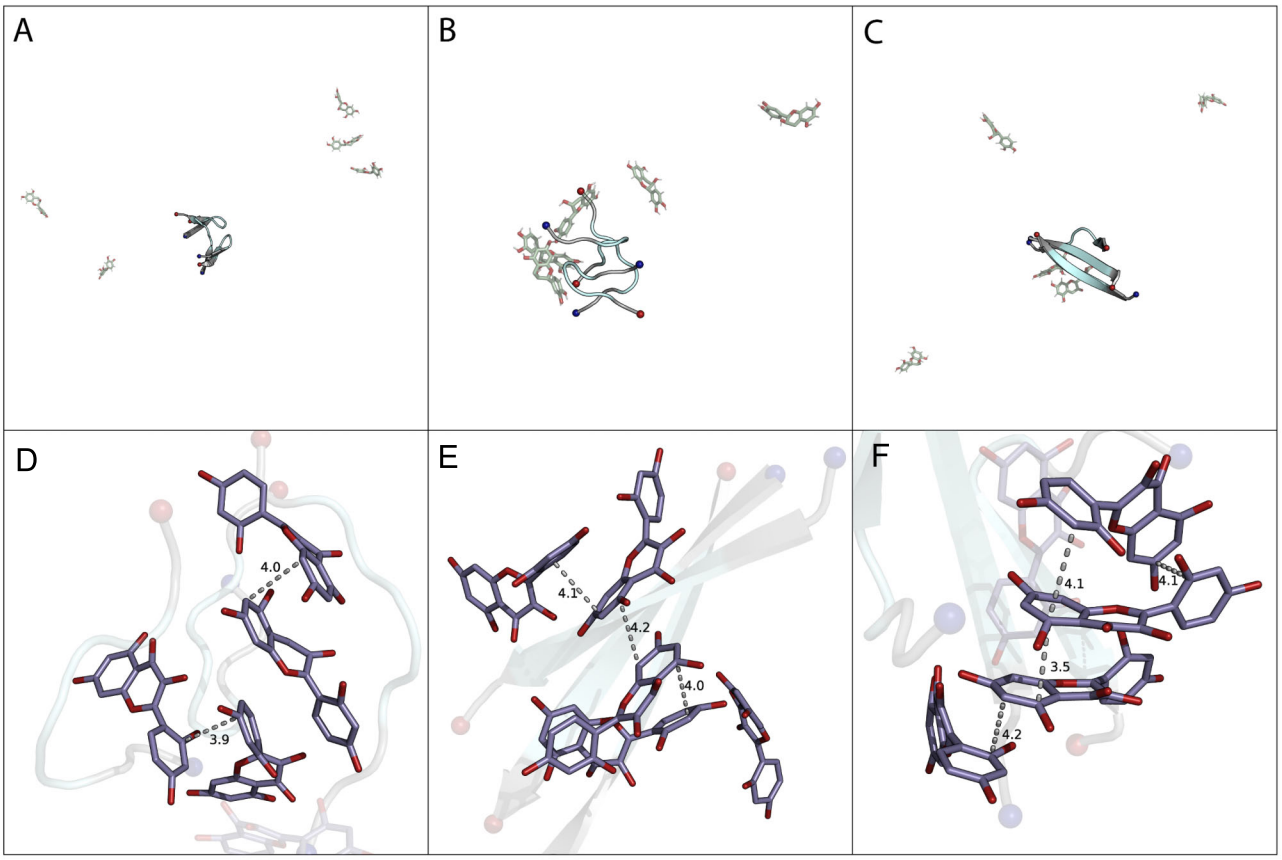

Figure S30: (A-C) Representative structures from RMSD clustering of $IAPP_{(20-29)}$ with epicatechin, showing epicatechin spread out in simulation box. Epicatechin colored green, and shown as sticks. **(D-F)** Representative structures from RMSD clustering of $IAPP_{(20-29)}$ with morin. Morin shows propensity to stack via B-ring. Morin colored purple, shown as sticks. Distance measurements are in Angstroms. **(A-F)** $IAPP_{(20-29)}$ peptides are shown as cartoon, with residues 23-27 (FGAIL) colored teal. N- and C-termini are colored blue and red, respectively, and shown as spheres.

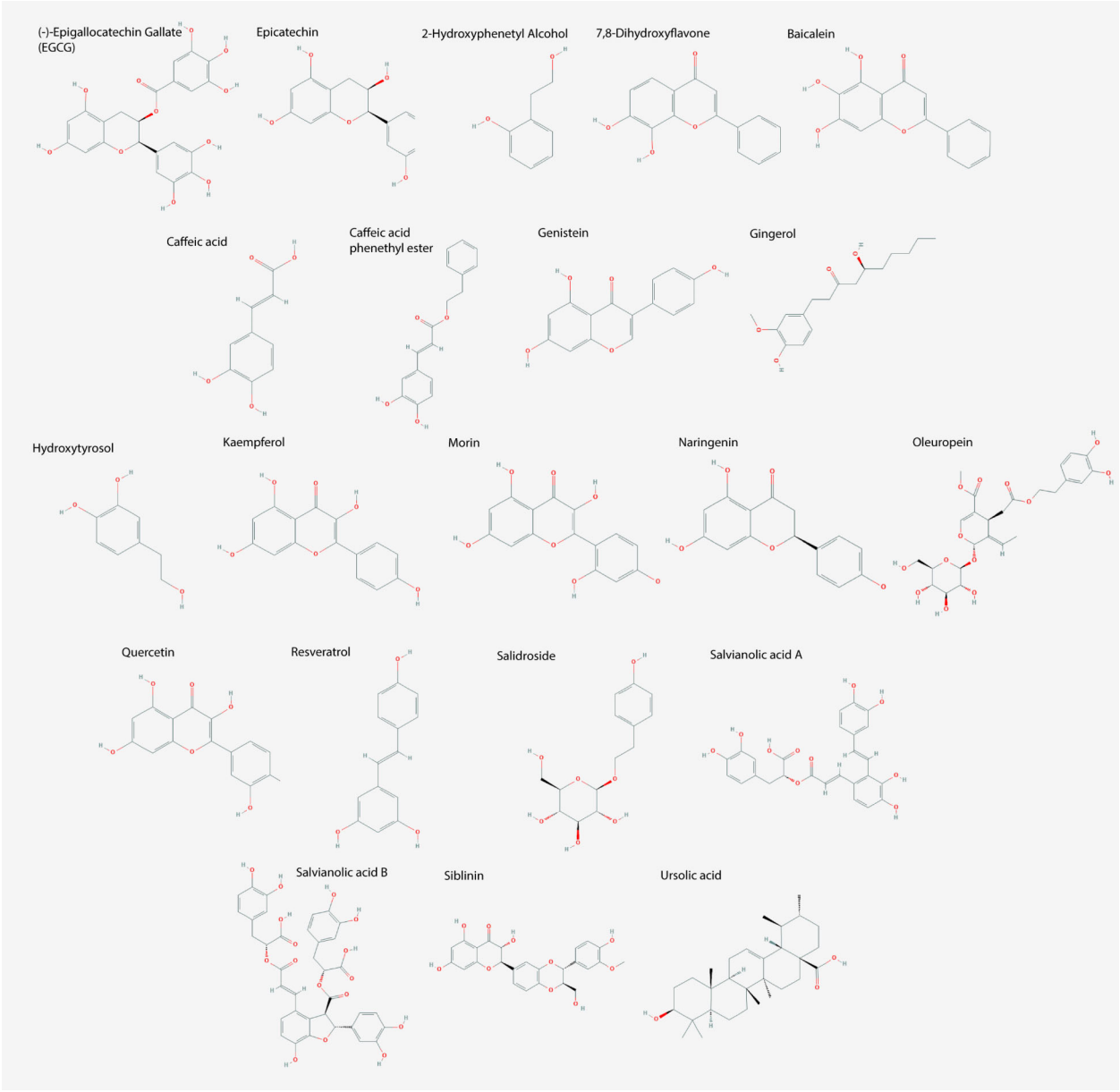

Figure S31: 2D structures of compounds used for data generation in section 3. Structures were downloaded from PubChem.

5 References

[1] Eisenberg, D., and Jucker, M. (2012) The amyloid state of proteins in human diseases, *Cell 148*, 1188-1203.

[2] Rambaran, R. N., and Serpell, L. C. (2008) Amyloid fibrils: abnormal protein assembly, *Prion 2*, 112-117.

[3] Haataja, L., Gurlo, T., Huang, C. J., and Butler, P. C. (2008) Islet Amyloid in Type 2 Diabetes, and the Toxic Oligomer Hypothesis, *Endocrine Reviews 29*, 303-316.

[4] Palato, L. M., Pilcher, S., Oakes, A., Lamba, A., Torres, J., Ledesma Monjaraz, L. I., Munoz, C., Njoo, E., Rinauro, D. J., Menefee, K. A., Tun, A., Jauregui, B. L., Shapiro, S., Nossiff, O. H., Olivares, E., Chang, K., Nguyen, V., Nogaj, L. A., and Moffet, D. A. (2019) Amyloidogenicity of naturally occurring full-length animal IAPP variants, *J Pept Sci 25*, e3199-e3199.

[5] Höppener, J. W., and Lips, C. J. (2006) Role of islet amyloid in type 2 diabetes mellitus, *Int J Biochem Cell Biol 38*, 726-736.

[6] Lutz, T. A. (2006) Amylinergic control of food intake, *Physiol Behav 89*, 465-471.

[7] Clementi, G., Caruso, A., Cutuli, V. M., de Bernardis, E., Prato, A., and Amico-Roxas, M. (1996) Amylin given by central or peripheral routes decreases gastric emptying and intestinal transit in the rat, *Experientia 52*, 677-679.

[8] Riediger, T., Zuend, D., Becskei, C., and Lutz, T. A. (2004) The anorectic hormone amylin contributes to feeding-related changes of neuronal activity in key structures of the gut-brain axis, *American Journal of Physiology-Regulatory, Integrative and Comparative Physiology 286*, R114-R122.

[9] Mosselman, S., Höppener, J. W., Lips, C. J., and Jansz, H. S. (1989) The complete islet amyloid polypeptide precursor is encoded by two exons, *FEBS letters 247*, 154-158.

[10] Westermark, P. (2011) Amyloid in the islets of Langerhans: thoughts and some historical aspects, *Ups J Med Sci 116*, 81-89.

[11] Sanke, T., Bell, G. I., Sample, C., Rubenstein, A. H., and Steiner, D. F. (1988) An islet amyloid peptide is derived from an 89-amino acid precursor by proteolytic processing, *The Journal of biological chemistry 263*, 17243-17246.

[12] Westermark, P., Wernstedt, C., Wilander, E., Hayden, D. W., O'Brien, T. D., and Johnson, K. H. (1987) Amyloid fibrils in human insulinoma and islets of Langerhans of the diabetic cat are derived from a neuropeptide-like protein also present in normal islet cells, *Proceedings of the National Academy of Sciences of the United States of America 84*, 3881-3885.

[13] Westermark, P., Engström, U., Johnson, K. H., Westermark, G. T., and Betsholtz, C. (1990) Islet amyloid polypeptide: pinpointing amino acid residues linked to amyloid fibril formation, *Proceedings of the National Academy of Sciences of the United States of America 87*, 5036-5040.

[14] Lorenzo, A., Razzaboni, B., Weir, G. C., and Yankner, B. A. (1994) Pancreatic islet cell toxicity of amylin associated with type-2 diabetes mellitus, *Nature 368*, 756-760.

[15] Janson, J., Ashley, R. H., Harrison, D., McIntyre, S., and Butler, P. C. (1999) The mechanism of islet amyloid polypeptide toxicity is membrane disruption by intermediate-sized toxic amyloid particles, *Diabetes 48*, 491-498.

[16] Anguiano, M., Nowak, R. J., and Lansbury, P. T. (2002) Protofibrillar Islet Amyloid Polypeptide Permeabilizes Synthetic Vesicles by a Pore-like Mechanism that May Be Relevant to Type II Diabetes, *Biochemistry 41*, 11338-11343.
[17] Mirzabekov, T. A., Lin, M. C., and Kagan, B. L. (1996) Pore formation by the cytotoxic islet amyloid peptide amylin, *J Biol Chem 271*, 1988-1992.
[18] Orrenius, S., Zhivotovsky, B., and Nicotera, P. (2003) Regulation of cell death: the calcium–apoptosis link, *Nature Reviews Molecular Cell Biology 4*, 552-565.
[19] Tzotzos, S., and Doig, A. J. (2010) Amyloidogenic sequences in native protein structures, *Protein Sci 19*, 327-348.
[20] Azriel, R., and Gazit, E. (2001) Analysis of the minimal amyloid-forming fragment of the islet amyloid polypeptide. An experimental support for the key role of the phenylalanine residue in amyloid formation, *The Journal of biological chemistry 276*, 34156-34161.
[21] Buchanan, L. E., Dunkelberger, E. B., Tran, H. Q., Cheng, P. N., Chiu, C. C., Cao, P., Raleigh, D. P., de Pablo, J. J., Nowick, J. S., and Zanni, M. T. (2013) Mechanism of IAPP amyloid fibril formation involves an intermediate with a transient beta-sheet, *Proceedings of the National Academy of Sciences of the United States of America 110*, 19285-19290.
[22] Wei, L., Jiang, P., Xu, W., Li, H., Zhang, H., Yan, L., Chan-Park, M. B., Liu, X.-W., Tang, K., Mu, Y., and Pervushin, K. (2011) The molecular basis of distinct aggregation pathways of islet amyloid polypeptide, *The Journal of biological chemistry 286*, 6291-6300.
[23] Cao, P., Meng, F., Abedini, A., and Raleigh, D. P. (2010) The ability of rodent islet amyloid polypeptide to inhibit amyloid formation by human islet amyloid polypeptide has important implications for the mechanism of amyloid formation and the design of inhibitors, *Biochemistry 49*, 872-881.
[24] Del Rio, D., Rodriguez-Mateos, A., Spencer, J. P. E., Tognolini, M., Borges, G., and Crozier, A. (2013) Dietary (poly)phenolics in human health: structures, bioavailability, and evidence of protective effects against chronic diseases, *Antioxid Redox Signal 18*, 1818-1892.
[25] Choy, K. W., Murugan, D., Leong, X.-F., Abas, R., Alias, A., and Mustafa, M. R. (2019) Flavonoids as Natural Anti-Inflammatory Agents Targeting Nuclear Factor-Kappa B (NFκB) Signaling in Cardiovascular Diseases: A Mini Review, *Frontiers in Pharmacology 10*.
[26] Panche, A. N., Diwan, A. D., and Chandra, S. R. (2016) Flavonoids: an overview, *J Nutr Sci 5*, e47-e47.
[27] Hanhineva, K., Törrönen, R., Bondia-Pons, I., Pekkinen, J., Kolehmainen, M., Mykkänen, H., and Poutanen, K. (2010) Impact of dietary polyphenols on carbohydrate metabolism, *Int J Mol Sci 11*, 1365-1402.
[28] Sun, Q., Wedick, N. M., Tworoger, S. S., Pan, A., Townsend, M. K., Cassidy, A., Franke, A. A., Rimm, E. B., Hu, F. B., and van Dam, R. M. (2015) Urinary Excretion of Select Dietary Polyphenol Metabolites Is Associated with a Lower Risk of Type 2 Diabetes in Proximate but Not Remote Follow-Up in a Prospective Investigation in 2 Cohorts of US Women, *J Nutr 145*, 1280-1288.
[29] Cao, P., and Raleigh, D. P. (2012) Analysis of the inhibition and remodeling of islet amyloid polypeptide amyloid fibers by flavanols, *Biochemistry 51*, 2670-2683.

[30] Meng, F., Abedini, A., Plesner, A., Verchere, C. B., and Raleigh, D. P. (2010) The Flavanol (−)-Epigallocatechin 3-Gallate Inhibits Amyloid Formation by Islet Amyloid Polypeptide, Disaggregates Amyloid Fibrils, and Protects Cultured Cells against IAPP-Induced Toxicity, *Biochemistry 49*, 8127-8133.
[31] Young, L. M., Cao, P., Raleigh, D. P., Ashcroft, A. E., and Radford, S. E. (2014) Ion Mobility Spectrometry–Mass Spectrometry Defines the Oligomeric Intermediates in Amylin Amyloid Formation and the Mode of Action of Inhibitors, *Journal of the American Chemical Society 136*, 660-670.
[32] Velander, P., Wu, L., Ray, W. K., Helm, R. F., and Xu, B. (2016) Amylin Amyloid Inhibition by Flavonoid Baicalein: Key Roles of Its Vicinal Dihydroxyl Groups of the Catechol Moiety, *Biochemistry 55*, 4255-4258.
[33] Velander, P., Wu, L., Henderson, F., Zhang, S., Bevan, D. R., and Xu, B. (2017) Natural product-based amyloid inhibitors, *Biochemical pharmacology 139*, 40-55.
[34] Noor, H., Cao, P., and Raleigh, D. P. (2012) Morin hydrate inhibits amyloid formation by islet amyloid polypeptide and disaggregates amyloid fibers, *Protein Sci 21*, 373-382.
[35] Sparks, S., Liu, G., Robbins, K. J., and Lazo, N. D. (2012) Curcumin modulates the self-assembly of the islet amyloid polypeptide by disassembling α-helix, *Biochem Biophys Res Commun 422*, 551-555.
[36] Ehrnhoefer, D. E., Bieschke, J., Boeddrich, A., Herbst, M., Masino, L., Lurz, R., Engemann, S., Pastore, A., and Wanker, E. E. (2008) EGCG redirects amyloidogenic polypeptides into unstructured, off-pathway oligomers, *Nature Structural & Molecular Biology 15*, 558-566.
[37] Sato, M., Murakami, K., Uno, M., Nakagawa, Y., Katayama, S., Akagi, K.-i., Masuda, Y., Takegoshi, K., and Irie, K. (2013) Site-specific Inhibitory Mechanism for Amyloid β42 Aggregation by Catechol-type Flavonoids Targeting the Lys Residues*, *Journal of Biological Chemistry 288*, 23212-23224.
[38] Zhu, M., Rajamani, S., Kaylor, J., Han, S., Zhou, F., and Fink, A. L. (2004) The Flavonoid Baicalein Inhibits Fibrillation of α-Synuclein and Disaggregates Existing Fibrils*, *Journal of Biological Chemistry 279*, 26846-26857.
[39] Palhano, F. L., Lee, J., Grimster, N. P., and Kelly, J. W. (2013) Toward the Molecular Mechanism(s) by Which EGCG Treatment Remodels Mature Amyloid Fibrils, *Journal of the American Chemical Society 135*, 7503-7510.
[40] Hudson, S. A., Ecroyd, H., Dehle, F. C., Musgrave, I. F., and Carver, J. A. (2009) (−)-Epigallocatechin-3-Gallate (EGCG) Maintains κ-Casein in Its Pre-Fibrillar State without Redirecting Its Aggregation Pathway, *Journal of Molecular Biology 392*, 689-700.
[41] Porat, Y., Abramowitz, A., and Gazit, E. (2006) Inhibition of amyloid fibril formation by polyphenols: structural similarity and aromatic interactions as a common inhibition mechanism, *Chemical biology & drug design 67*, 27-37.
[42] Gazit, E. (2002) A possible role for π-stacking in the self-assembly of amyloid fibrils, *The FASEB Journal 16*, 77-83.
[43] Berhanu, W. M., and Masunov, A. E. (2015) Atomistic mechanism of polyphenol amyloid aggregation inhibitors: molecular dynamics study of Curcumin, Exifone, and Myricetin interaction with the segment of tau peptide oligomer, *Journal of Biomolecular Structure and Dynamics 33*, 1399-1411.
[44] Cao, P., and Raleigh, D. P. (2012) Analysis of the inhibition and remodeling of islet amyloid polypeptide amyloid fibers by flavanols, *Biochemistry 51*, 2670-2683.

[45] Rao, P. P. N., Mohamed, T., Teckwani, K., and Tin, G. (2015) Curcumin Binding to Beta Amyloid: A Computational Study, *Chemical biology & drug design 86*, 813-820.
[46] Ma, B., and Nussinov, R. (2006) Simulations as analytical tools to understand protein aggregation and predict amyloid conformation, *Curr Opin Chem Biol 10*, 445-452.
[47] Zheng, J., Ma, B., Tsai, C. J., and Nussinov, R. (2006) Structural stability and dynamics of an amyloid-forming peptide GNNQQNY from the yeast prion sup-35, *Biophys J 91*, 824-833.
[48] Forouhi, N. G., and Wareham, N. J. (2014) Epidemiology of diabetes, *Medicine (Abingdon) 42*, 698-702.
[49] Organzation, W. H. (2016)
Global Report on Diabetes.
[50] Abdul-Ghani, M. A., and DeFronzo, R. A. (2009) Plasma glucose concentration and prediction of future risk of type 2 diabetes, *Diabetes Care 32 Suppl 2*, S194-S198.
[51] Weir, G. C., and Bonner-Weir, S. (2004) Five stages of evolving beta-cell dysfunction during progression to diabetes, *Diabetes 53 Suppl 3*, S16-21.
[52] Clark, A., Edwards, C. A., Ostle, L. R., Sutton, R., Rothbard, J. B., Morris, J. F., and Turner, R. C. (1989) Localisation of islet amyloid peptide in lipofuscin bodies and secretory granules of human B-cells and in islets of type-2 diabetic subjects, *Cell and Tissue Research 257*, 179-185.
[53] Hartter, E., Svoboda, T., Ludvik, B., Schuller, M., Lell, B., Kuenburg, E., Brunnbauer, M., Woloszczuk, W., and Prager, R. (1991) Basal and stimulated plasma levels of pancreatic amylin indicate its co-secretion with insulin in humans, *Diabetologia 34*, 52-54.
[54] Laybutt, D. R., Glandt, M., Xu, G., Ahn, Y. B., Trivedi, N., Bonner-Weir, S., and Weir, G. C. (2003) Critical Reduction in β-Cell Mass Results in Two Distinct Outcomes over Time: ADAPTATION WITH IMPAIRED GLUCOSE TOLERANCE OR DECOMPENSATED DIABETES*, *Journal of Biological Chemistry 278*, 2997-3005.
[55] Levy, J., Atkinson, A. B., Bell, P. M., McCance, D. R., and Hadden, D. R. (1998) Beta-cell deterioration determines the onset and rate of progression of secondary dietary failure in type 2 diabetes mellitus: the 10-year follow-up of the Belfast Diet Study, *Diabet Med 15*, 290-296.
[56] Fonseca, V. A. (2009) Defining and characterizing the progression of type 2 diabetes, *Diabetes Care 32 Suppl 2*, S151-S156.
[57] Liu, C., Zhao, M., Jiang, L., Cheng, P.-N., Park, J., Sawaya, M. R., Pensalfini, A., Gou, D., Berk, A. J., Glabe, C. G., Nowick, J., and Eisenberg, D. (2012) Out-of-register β-sheets suggest a pathway to toxic amyloid aggregates, *Proceedings of the National Academy of Sciences 109*, 20913-20918.
[58] De Vivo, M., Masetti, M., Bottegoni, G., and Cavalli, A. (2016) Role of Molecular Dynamics and Related Methods in Drug Discovery, *Journal of Medicinal Chemistry 59*, 4035-4061.
[59] Hess, B., Kutzner, C., van der Spoel, D., and Lindahl, E. (2008) GROMACS 4: Algorithms for Highly Efficient, Load-Balanced, and Scalable Molecular Simulation, *Journal of Chemical Theory and Computation 4*, 435-447.
[60] Oostenbrink, C., Villa, A., Mark, A. E., and van Gunsteren, W. F. (2004) A biomolecular force field based on the free enthalpy of hydration and solvation: the GROMOS force-field parameter sets 53A5 and 53A6, *Journal of computational chemistry 25*, 1656-1676.

[61] Nanga, R. P., Brender, J. R., Vivekanandan, S., and Ramamoorthy, A. (2011) Structure and membrane orientation of IAPP in its natively amidated form at physiological pH in a membrane environment, *Biochimica et biophysica acta 1808*, 2337-2342.
[62] Wu, L., Velander, P., Brown, A. M., Wang, Y., Liu, D., Bevan, D. R., Zhang, S., and Xu, B. (2020) Catechol-Containing Compounds are a Broad Class of Protein Aggregation Inhibitors: II. Rosmarinic Acid Potently Detoxifies Amylin Amyloid and Ameliorates Diabetic Pathology in HIP Rats, *bioRxiv*, 2020.2012.2013.873687.
[63] Schüttelkopf, A. W., and van Aalten, D. M. (2004) PRODRG: a tool for high-throughput crystallography of protein-ligand complexes, *Acta Crystallogr D Biol Crystallogr 60*, 1355-1363.
[64] Lemkul, J. A., and Bevan, D. R. (2010) Destabilizing Alzheimer's Aβ42 Protofibrils with Morin: Mechanistic Insights from Molecular Dynamics Simulations, *Biochemistry 49*, 3935-3946.
[65] Stubbs, J. M., Potoff, J. J., and Siepmann, J. I. (2004) Transferable Potentials for Phase Equilibria. 6. United-Atom Description for Ethers, Glycols, Ketones, and Aldehydes, *The Journal of Physical Chemistry B 108*, 17596-17605.
[66] The PyMOL Molecular Graphics System, Version 2.0 Schrödinger, LLC.
[67] Berendsen, H. J. C., Postma, J. P. M., van Gunsteren, W., and Hermans, J. (2019) *Interaction models for water in relation to protein hydration in Intermolecular forces*.
[68] Berendsen, H. J. C., Postma, J. P. M., Gunsteren, W. F. v., DiNola, A., and Haak, J. R. (1984) MOLECULAR-DYNAMICS WITH COUPLING TO AN EXTERNAL BATH.
[69] Nosé, S. (1984) A molecular dynamics method for simulations in the canonical ensemble, *Molecular Physics 52*, 255-268.
[70] Hoover, W. G. (1985) Canonical dynamics: Equilibrium phase-space distributions, *Physical Review A 31*, 1695-1697.
[71] Paci, E., and Marchi, M. (1996) Constant-Pressure Molecular Dynamics Techniques Applied to Complex Molecular Systems and Solvated Proteins, *The Journal of Physical Chemistry 100*, 4314-4322.
[72] Parrinello, M. R. A., and Rahman, A. J. (1982) *Polymorphic Transitions in Single Crystals: A New Molecular Dynamics Method*, Vol. 52.
[73] Hess, B., Bekker, H., Berendsen, H., and G. E. M. Fraaije, J. (1998) *LINCS: A Linear Constraint Solver for molecular simulations*, Vol. 18.
[74] Darden, T., York, D., and Pedersen, L. (1993) *Particle Mesh Ewald: An Nlog (N) Method for Ewald Sums in Large Systems*, Vol. 98.
[75] Essmann, U., Perera, L., Berkowitz, M. L., Darden, T., Lee, H., and Pedersen, L. G. (1995) A smooth particle mesh Ewald method, *The Journal of Chemical Physics 103*, 8577-8593.
[76] Brown, A. M., Briganti, J., Sharp, A., Kelly, C., Gottschalk, C., and King, K. M. (2021) Bevan & Brown Lab, Public.
[77] Abraham, M. J., Murtola, T., Schulz, R., Páll, S., Smith, J. C., Hess, B., and Lindahl, E. (2015) GROMACS: High performance molecular simulations through multi-level parallelism from laptops to supercomputers, *SoftwareX 1-2*, 19-25.
[78] Daura, X., van Gunsteren, W. F., and Mark, A. E. (1999) Folding–unfolding thermodynamics of a β-heptapeptide from equilibrium simulations, *Proteins: Structure, Function, and Bioinformatics 34*, 269-280.
[79] 2021-1, S. R. QikProp, Schrödinger, LLC, New York, NY, 2021.

[80] Gerben, S. R., Lemkul, J. A., Brown, A. M., and Bevan, D. R. (2014) Comparing atomistic molecular mechanics force fields for a difficult target: a case study on the Alzheimer's amyloid β-peptide, *Journal of Biomolecular Structure and Dynamics 32*, 1817-1832.
[81] Sunde, M., and Blake, C. C. F. (1998) From the globular to the fibrous state: protein structure and structural conversion in amyloid formation, *Quarterly Reviews of Biophysics 31*, 1-39.
[82] Ge, X., Yang, Y., Sun, Y., Cao, W., and Ding, F. (2018) Islet Amyloid Polypeptide Promotes Amyloid-Beta Aggregation by Binding-Induced Helix-Unfolding of the Amyloidogenic Core, *ACS chemical neuroscience 9*, 967-975.
[83] Fawver, J. N., Ghiwot, Y., Koola, C., Carrera, W., Rodriguez-Rivera, J., Hernandez, C., Dineley, K. T., Kong, Y., Li, J., Jhamandas, J., Perry, G., and Murray, I. V. (2014) Islet amyloid polypeptide (IAPP): a second amyloid in Alzheimer's disease, *Curr Alzheimer Res 11*, 928-940.
[84] Tang, Y., Liu, Y., Zhang, Y., Zhang, D., Gong, X., and Zheng, J. (2021) Repurposing a Cardiovascular Disease Drug of Cloridarol as hIAPP Inhibitor, *ACS Chemical Neuroscience*.
[85] Kabsch, W., and Sander, C. (1983) Dictionary of protein secondary structure: pattern recognition of hydrogen-bonded and geometrical features, *Biopolymers 22*, 2577-2637.
[86] Porat, Y., Mazor, Y., Efrat, S., and Gazit, E. (2004) Inhibition of islet amyloid polypeptide fibril formation: a potential role for heteroaromatic interactions, *Biochemistry 43*, 14454-14462.
[87] Tracz, S. M., Abedini, A., Driscoll, M., and Raleigh, D. P. (2004) Role of Aromatic Interactions in Amyloid Formation by Peptides Derived from Human Amylin, *Biochemistry 43*, 15901-15908.
[88] Tu, L.-H., and Raleigh, D. P. (2013) Role of Aromatic Interactions in Amyloid Formation by Islet Amyloid Polypeptide, *Biochemistry 52*, 333-342.
[89] Marek, P., Abedini, A., Song, B., Kanungo, M., Johnson, M. E., Gupta, R., Zaman, W., Wong, S. S., and Raleigh, D. P. (2007) Aromatic Interactions Are Not Required for Amyloid Fibril Formation by Islet Amyloid Polypeptide but Do Influence the Rate of Fibril Formation and Fibril Morphology, *Biochemistry 46*, 3255-3261.
[90] Aarabi, M.-H., and Mirhashemi, S. M. (2012) The role of two natural flavonoids on human amylin aggregation, *African Journal of Pharmacy and Pharmacology 6*.
[91] Porat, Y., Mazor, Y., Efrat, S., and Gazit, E. (2004) Inhibition of Islet Amyloid Polypeptide Fibril Formation: A Potential Role for Heteroaromatic Interactions, *Biochemistry 43*, 14454-14462.
[92] Tu, L.-H., Young, L. M., Wong, A. G., Ashcroft, A. E., Radford, S. E., and Raleigh, D. P. (2015) Mutational Analysis of the Ability of Resveratrol To Inhibit Amyloid Formation by Islet Amyloid Polypeptide: Critical Evaluation of the Importance of Aromatic–Inhibitor and Histidine–Inhibitor Interactions, *Biochemistry 54*, 666-676.
[93] Bochevarov, A. D., Harder, E., Hughes, T. F., Greenwood, J. R., Braden, D. A., Philipp, D. M., Rinaldo, D., Halls, M. D., Zhang, J., and Friesner, R. A. (2013) Jaguar: A high-performance quantum chemistry software program with strengths in life and materials sciences, *International Journal of Quantum Chemistry 113*, 2110-2142.
[94] Jain, A., Purohit, C. S., Verma, S., and Sankararamakrishnan, R. (2007) Close Contacts between Carbonyl Oxygen Atoms and Aromatic Centers in Protein Structures: π···π or Lone-Pair···π Interactions?, *The Journal of Physical Chemistry B 111*, 8680-8683.

[95] Feng, B. Y., Toyama, B. H., Wille, H., Colby, D. W., Collins, S. R., May, B. C., Prusiner, S. B., Weissman, J., and Shoichet, B. K. (2008) Small-molecule aggregates inhibit amyloid polymerization, *Nature chemical biology 4*, 197-199.
[96] Nedumpully-Govindan, P., Kakinen, A., Pilkington, E. H., Davis, T. P., Chun Ke, P., and Ding, F. (2016) Stabilizing Off-pathway Oligomers by Polyphenol Nanoassemblies for IAPP Aggregation Inhibition, *Scientific Reports 6*, 19463.
[97] Tycko, R. (2006) Molecular structure of amyloid fibrils: insights from solid-state NMR, *Quarterly Reviews of Biophysics 39*, 1-55.
[98] Pithadia, A., Brender, J. R., Fierke, C. A., and Ramamoorthy, A. (2016) Inhibition of IAPP Aggregation and Toxicity by Natural Products and Derivatives, *J Diabetes Res 2016*, 2046327-2046327.
[99] Ioakimidis, L., Thoukydidis, L., Mirza, A., Naeem, S., and Reynisson, J. (2008) Benchmarking the Reliability of QikProp. Correlation between Experimental and Predicted Values, *QSAR & Combinatorial Science 27*, 445-456.
[100] Wang, Y., Lv, Y., Jin, L., and Liang, G. (2020) Revealing the Mechanism of EGCG, Genistein, Rutin, Quercetin, and Silibinin Against hIAPP Aggregation via Computational Simulations, *Interdisciplinary Sciences: Computational Life Sciences 12*, 59-68.
[101] Roy, R., and Paul, S. (2020) Theoretical Investigation of the Inhibitory Mechanism of Norepinephrine on hIAPP Amyloid Aggregation and the Destabilization of Protofibrils, *The Journal of Physical Chemistry B 124*, 10913-10929.